Journal of Non-Crystalline Solids 600 (2023) 122020

Contents lists available at ScienceDirect

Journal of Non-Crystalline Solids

journal homepage: www.elsevier.com/locate/jnoncrysol

Structure-terahertz property relationship and femtosecond laser irradiation effects in chalcogenide glasses

Nicholas J. Tostanoski [a,*], Edwin J. Heilweil [b], Peter F. Wachtel [c], J. David Musgraves [c], S. K. Sundaram [a]

[a] Terahertz Waves Science and Technology Laboratory (T-Lab), Inamori School of Engineering, the New York State College of Ceramics, Alfred University, Alfred, NY 14802, USA
[b] National Institute of Standards and Technology, Gaithersburg, MD 20899, USA
[c] Rochester Precision Optics LLC, 850 John Street, Rochester NY 14586, USA

ARTICLE INFO

Keywords:
Chalcogenide Glasses
Structure-property relationship
Raman spectroscopy
Terahertz time-domain spectroscopy
Femtosecond laser irradiation

ABSTRACT

We report structure-terahertz (THz) property relationship for various non-oxide chalcogenide glasses including unary (vitreous selenium (Se)), binary (arsenic sulfide (As-S), arsenic selenide (As-Se), and germanium selenide (Ge-Se)), and ternary (germanium arsenic selenide (Ge-As-Se)), systems along with commercially available AMTIR-1, IRG 22, and IRG 24 Ge-As-Se glasses. This comprehensive study is the first of its kind to combine Raman spectroscopy to examine structural units, connectivity, and glass network and terahertz time-domain spectroscopy (THz-TDS) to record the THz refractive index, n(THz), across a broad THz bandwidth. THz-TDS was carried out at Alfred University (AU) and National Institute of Standards and Technology (NIST), ultimately providing confidence in n(THz) values measured at AU. Vitreous Se, $<r> = 2.0$, record the minimum THz refractive index value of all Se-containing glasses. As-S and As-Se binary glasses have the highest measurable THz refractive index value at $<r> = 2.4$. Ge-Se binary glasses measure increased THz refractive index as $<r>$ increases, with the maximum at $<r> = 2.8$. Ternary Ge-As-Se glasses record the maximum THz refractive index value at $<r> = 2.5$ for $Ge_{10}As_{30}Se_{60}$. Low-repetition rate femtosecond laser irradiation (≈1 KHz, ≈40 fs, and ≈70 mW) was used to modify As-S and As-Se glass systems, where Raman and THz-TDS were used to observe minimal structural and THz refractive index values changes, respectively. Long-wave infrared (LWIR) (e.g., 10 μm)-THz (e.g., 1.0 THz) refractive index correlation is presented for all binary and ternary studied chalcogenide glasses. Such a correlation is valuable for predicting and designing chalcogenide glasses for integrated optical applications across THz and IR regions.

1. Introduction

Non-oxide chalcogenide glasses are composed of elemental materials including glass forming chalcogen (Ch) elements, e.g., S, Se, and Te, and additional tetrel or pnictogen elements, e.g., Ge or As. Covalent bonding between elements dominates the glass structure with Ge, As, and Ch elements found in four-, three-, and two-fold coordination, respectively. Fig. 1 shows representative structural units found in chalcogenide glasses. The coordination number follows the 8-N rule, where N is the number of outer shell (valence) electrons. Vitreous sulfur and selenium form covalently bonded chains (Ch_n) (Fig. 1 (a)) and rings (Ch_8) (Fig. 1 (b)) with Van der Waals forces acting between the structural units, described as 0- (e.g., rings) and 1-dimensional (e.g., chains) glass networks. Addition of As or Ge to S or Se results in increased connectivity of the glass network, promoting the transition into a 2- (e.g., sheets or layers) and 3-dimensional glass network with As pyramidal, $AsCh_{3/2}$ (Fig. 1 (c)), and Ge tetrahedral, $GeCh_{4/2}$ (Fig. 1 (d)), structural units connected via S or Se chains of various lengths, where $AsCh_{3/2}$ pyramids contain a lone pair of electrons. According to this nomenclature, structural units are referred to the number of atoms found in each unit, i.e., $AsCh_{3/2}$ pyramids and $GeCh_{4/2}$ tetrahedra indicates that each As and Ge atom are connected to three and four Ch atoms, respectively, that are each two-fold coordinated, identified by the /2 subscript, where each Ch atom is split between two structural units and serves as a bridging connection.

Average or mean coordination number, $<r>$, increases as the

* Corresponding author.
E-mail address: njt2@alfred.edu (Nicholas J. Tostanoski).

https://doi.org/10.1016/j.jnoncrysol.2022.122020
Received 9 August 2022; Received in revised form 12 October 2022; Accepted 6 November 2022
Available online 12 November 2022

connectivity of the glass structure increases through addition of higher coordinated elements. <r> is defined as the weighted coordination of component elements/atoms within the glass, it is typically used to describe the structure and therefore resulting properties of the glass. Vitreous S and Se have <r> of 2, where addition of other elements, e.g., Ge and As, results in an increase in <r>, connectivity, and crosslinking of the glass network. The average coordination number, <r>, is calculated by using the equation reflecting four-, three-, and two-fold coordination of Ge, As, and S and Se, respectively:

$$\langle r \rangle = 4\left(\frac{\%Ge}{100}\right) + 3\left(\frac{\%As}{100}\right) + 2\left(\frac{\%S}{100}\right) + 2\left(\frac{\%Se}{100}\right)$$

Phillips [1], Thorpe [2], and later Phillips and Thorpe [3] proposed the topological constraint theory to assist in describing glass formation based on bonding constraints and degrees of freedom for a glass network of a defined glass composition. Where glass networks of <r> less than 2.4 and <r> greater than 2.4 are considered floppy or "under-constrained" and rigid or "over-constrained", respectively. An <r> = 2.4 is the ideal coordination of glass structure, that resists crystallization and has the most/ideal connected glass network or "optimally-constrained" and are the best glass forming compositions, where the number of constraints is equal to the number of degrees of freedom [1–5].

Chalcogenide glasses, e.g., As-S, As-Se, and Ge-Se binary glass systems, e.g., such as As_2S_3, As_2Se_3, and $GeSe_2$, and Ge-As-Se ternary systems, e.g., commercially available AMTIR 1, IRG 22, and IRG 24, are often used in IR applications due to their specific optical properties [6]. Chalcogenide glasses have superior optical properties, while also possessing inferior mechanical and thermal properties, in comparison to more traditional glasses, e.g., silicate, borate, borosilicate, and phosphate glass systems, including a wide transparency window across the infrared (IR) region, including the long-wave infrared (LWIR) region of the electromagnetic spectrum from 8 to 12 μm [7–10], high refractive index [7,11–15] provided in Table 1, high nonlinear optical properties [7], and low refractive index dispersion [7,11–15]. Chalcogenide glasses have reduced ultraviolet (UV) and visible (Vis) transmission due to electronic transitions occurring at the optical bandgap. Increased IR transmission window is due to fundamental vibrational modes occurring at lower frequencies for heavier elements in chalcogenide glasses. These properties allow chalcogenide glasses to be used in optical devices including thermal and infrared imaging [7,9,10], fiber optic amplifiers, optical gratings [16], active optical devices including modulators and switching devices [8,16,17], and data/information storage [8].

Terahertz time-domain spectroscopy (THz-TDS) measures optical and dielectric constants at defined THz frequencies. It is widely known that THz refractive index values are greater than those found in the visible region of the electromagnetic spectrum for indices near their respective minimum dispersion wavelength/frequencies, due to electronic and ionic polarization mechanisms contributing to the total polarizability, this holds true for chalcogenide glasses. Previously, Naftaly et al. [19–22] reported THz refractive index and absorption spectra of various silicate glasses, concluding that glasses with constituents of higher polarizabilities, more ionic character, and a disordered network have larger measurable THz refractive index values. We have recently reported, for the first time, evidence of glass structure-THz property relationship in the sodium borosilicate glass system [23]. However, such a study has not been carried out for the chalcogenide glass family, with a few studies having reported THz refractive index values for chalcogenide glasses. Once such a relationship is established THz-TDS can become a powerful characterization technique for glasses [24]. It is suspected modification of THz refractive indices occurs with femtosecond laser irradiation, which has been known to induce refractive index changes in the visible and IR regions. A brief review of femtosecond laser-glass interactions with a focus on chalcogenide glass systems is provided below and serves as a brief background to the reader.

Femtosecond laser systems are used in micromachining of precise 3-dimensional photonic components or for surface or bulk modification or of glasses resulting in structural, density, and refractive index changes [25]. Laser-matter interactions are dictated by glass composition, structure and properties and laser parameters including repetition rate. Low-repetition rates are on the order of 1 to 200 kHz with pulse energies of a few μJ and pulse widths between 50 and 200 fs, where focal volume modification occurs within a single pulse [25–30]. Absorption of incident photon energy by glasses occurs via nonlinear mechanisms, i.e., multiphoton ionization in which an electron absorbs energy from multiple incident photons transitioning from the valence to conduction band, overcoming the band gap energy. Musgraves et al. [31] reviewed mechanisms of laser-induced structural modification of various glass systems with a focus on femtosecond modification of chalcogenides.

Low-repetition rate material modification has produced low asymmetric refractive index changes on the order of 10^{-3} [26,29,30]. Refractive index modification for repetition rates greater than 50 kHz are associated with heat accumulation and corresponding glass melting and quenching, resulting in structural and refractive index changes [25–28]. Low-repetition rate femtosecond laser systems have been used to irradiate As-S [32,33], As-Se [32], and Ge-S [34], and multicomponent Ge-As-S [35], Ge-As-Se [36,37], Ge-S-In-S [34], Ge-Ga-As-S [38], and Ge-Ga-Sb-S-Se [39] chalcogenide glasses, primarily focused on reviewing damage mechanisms, laser damage threshold, glass stability, and microstructure modification of glasses for the purpose of femtosecond laser writing or micromachining for production of waveguides with refractive index changes, with minimal structural or THz (structure-THz) with femtosecond laser interaction studies carried out. Initially shown by Tanaka [40] and later confirmed by Efimov et al. [33], Raman spectra of laser exposed As-S glasses confirmed merging of bands, e.g., at ca. 223 and 236 cm^{-1} into a broad band, suggesting an increase in disorder of the network and photodarkening (PD) and broader distribution of bond lengths and angles. Efimov et al. [33] determined refractive index changes, on the order of 5×10^{-4}, in $As_{40}S_{60}$ was due to breaking stable heteropolar As-S bonds and photo-induced formation of As-As and S-S homopolar bonds, resulting in a more disordered glass network. Tanaka [41,42] reviewed bandgap excitations of As_2S_3 glass, one- and two-photon absorption of the same frequency produce PD and refractive index changes without PD,

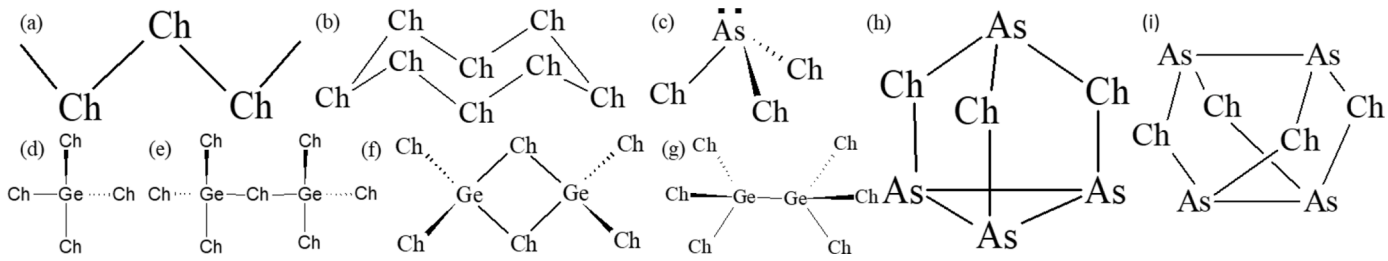

Fig. 1. Schematic of structural units found in various chalcogenide glasses, where Ch represents chalcogen S or Se atoms, including (a) Ch_n chain, (b) Ch_8 ring, (c) $AsCh_{3/2}$ pyramid with a lone pair of electrons, (d) $GeCh_{4/2}$ tetrahedra, (e) corner-sharing $GeCh_{4/2}$ tetrahedra, (f) edge-sharing $GeCh_{4/2}$ tetrahedra, (g) Ge-Ge homopolar bond in ethane-like $(Ch_3)Ge\text{-}Ge(Ch_3)$ units, (h) As_4Ch_3 molecular cage, and (i) As_4Ch_4 molecular cage.

Table 1
Experimental (nominal) vitreous selenium (Se), arsenic sulfide (As-S), arsenic selenide (As-Se), germanium selenide (Ge-Se), and germanium arsenic selenide (Ge-As-Se) glass compositions (at.%) with corresponding average coordination number (<r>), experimental 0.5 and 1.0 THz refractive index (n) and standard deviation (σ), and refractive index at defined long-wave infrared (LWIR) wavelength of 10 μm as reported in literature using a six variable Sellmeier equation.

Glass (at.%)	Ge (%)	As (%)	S (%)	Se (%)	<r>	n(0.5 THz)	σ(0.5 THz)	n(1.0 THz)	σ(1.0 THz)	n(10 μm)	Refs.
Se	-	-	-	100	2.00	2.4778	0.0128	2.4535	0.0168	-	-
$As_{15}S_{85}$	-	15	85	-	2.15	2.2156	0.0148	2.2104	0.0141	2.0482 *	[18]
$As_{20}S_{80}$	-	20	80	-	2.20	2.3306	0.0049	2.3234	0.0038	2.1132 *	[18]
$As_{25}S_{75}$	-	25	75	-	2.25	2.4376	0.0059	2.4274	0.0053	2.1781*	[18]
$As_{30}S_{70}$	-	30	70	-	2.30	2.5467	0.0052	2.5335	0.0054	2.2488	[18]
$As_{35}S_{65}$	-	35	65	-	2.35	2.6483	0.0088	2.6369	0.0081	2.3081*	[18]
$As_{40}S_{60}$	-	40	60	-	2.40	2.8166	0.0032	2.8037	0.0027	2.3762	[18]
$As_{10}Se_{90}$	-	10	-	90	2.10	2.6128	0.0116	2.5936	0.0110	2.4894	[11]
$As_{20}Se_{80}$	-	20	-	80	2.20	2.7816	0.0079	2.7649	0.0052	2.5811	[11]
$As_{30}Se_{70}$	-	30	-	70	2.30	2.9013	0.0170	2.8768	0.0203	2.6598	[11]
$As_{40}Se_{60}$	-	40	-	60	2.40	3.1342	0.0018	3.1131	0.0021	2.7781	[11]
$As_{50}Se_{50}$	-	50	-	50	2.50	2.9278	0.0016	2.9057	0.0019	- ◆	-
$As_{60}Se_{40}$	-	60	-	40	2.60	2.7311	0.0026	2.7062	0.0022	- ◆	-
$Ge_{10}Se_{90}$	10	-	-	90	2.20	2.6093	0.0071	2.5941	0.0049	2.4225	[11]
$Ge_{20}Se_{80}$	20	-	-	80	2.40	2.6899	0.0040	2.6808	0.0063	2.3942	[11]
$Ge_{30}Se_{70}$	30	-	-	70	2.60	2.7169	0.0072	2.7000	0.0044	2.3529	[11]
$Ge_{40}Se_{60}$	40	-	-	60	2.80	2.9024	0.0116	2.8948	0.0248	2.4865	[11]
$Ge_{10}As_{10}Se_{80}$	10	10	-	80	2.30	2.7114	0.0153	2.6871	0.0206	2.4924	[11]
$Ge_{10}As_{20}Se_{70}$	10	20	-	70	2.40	2.8996	0.0065	2.8886	0.0051	2.5508	[11]
$Ge_{20}As_{10}Se_{70}$	20	10	-	70	2.50	2.8410	0.0115	2.8300	0.0138	2.5037	[11]
$Ge_{10}As_{30}Se_{60}$	10	30	-	60	2.50	3.0116	0.0103	2.9900	0.0115	2.6080	[11]
$Ge_{20}As_{20}Se_{60}$	20	20	-	60	2.60	2.8153	0.0238	2.8240	0.0175	2.4911	[11]
$Ge_{30}As_{10}Se_{60}$	30	10	-	60	2.70	2.7282	0.0261	2.7336	0.0255	2.4265	[11]
AMTIR 1	33	12	-	55	2.78	2.8732	0.0006	2.8898	0.0013	2.4981	[12]
IRG 22	33	12	-	55	2.78	2.8583	0.0014	2.8684	0.0023	2.4968	[14]
IRG 24	10	40	-	50	2.60	2.8944	0.0005	2.8847	0.0014	2.6090	[15]

* Extrapolation of select As-S glass n(10 μm) from interpolated refractive index range using Sellmeier parameters from Ref. [18].
◆ It is not appropriate to extrapolate n(10 μm) from interpolated refractive index range using Sellmeier parameters due to <r> trend, it is suspected when <r> increases beyond 2.4 that n(10 μm) decreases.

respectively. Petit et al. [43] systemically studied the Ge-Sb-S/Se system suggesting laser irradiation promotes connectivity of GeS_4 units through forming corner sharing $GeSe_{4/2}$ units, S-S bridges, and homopolar S-S and Se-Se bonds. Petit et al. [44] reviewed the photoresponse of As- and Ge-S glass films where laser exposure of As- and Ge-based glasses results in As network bond dissociation and network bond rearrangement with positive and negative changes in the refractive index, respectively, and includes PD and photobleaching (PB). Sundaram et al. [45] reviewed accumulated gamma radiation doses effects on the structure and optical properties of As-S binary chalcogenide glasses.

Our work aims to review and advance structure-THz property relationship within the non-oxide vitreous selenium (Se), arsenic sulfide (As-S), arsenic selenide (As-Se), germanium selenide (Ge-Se), and germanium arsenic selenide (Ge-As-Se) chalcogenide glass systems. Such a relationship and correlations will be beneficial for predicting and controlling optical properties for integrated THz photonics and potentially dual mode across THz and long-wave infrared (LWIR) regions. A low-repetition rate femtosecond laser system with 800 nm wavelength output was used to irradiate and modify the glass structure. Raman spectroscopy was used to provide insight into short- and intermediate-range order of the glass structure, connectivity, and network of pristine and laser irradiated chalcogenide glasses and THz-TDS applied to determine the refractive index at THz frequencies of pristine and laser irradiated glasses. Measured THz-TDS refractive indices at Alfred University (AU) was evaluated through THz-TDS of As-S and As-Se at National Institute of Standards and Technology (NIST), ultimately providing confidence in measured THz refractive indices. LWIR-THz refractive index correlation of chalcogenide glass families is presented with structure-property relationships developed within the chalcogenide glass systems studied.

2. Experimental procedure[1]

Vitreous selenium (Se), arsenic sulfide (As-S), arsenic selenide (As-Se), germanium selenide (Ge-Se), and germanium arsenic selenide (Ge-As-Se) families of unary, binary, and ternary chalcogenide glasses were produced and processed at Rochester Precision Optics (RPO), discussed in detail elsewhere [11]. Commercial Ge-As-Se AMTIR 1 (amorphous material transmitting infrared radiation) ($Ge_{33}As_{12}Se_{55}$), IRG 22 ($Ge_{33}As_{12}Se_{55}$), and IRG 24 ($Ge_{10}As_{40}Se_{50}$) ternary chalcogenide glasses were acquired from Amorphous Materials [12] and Schott [14,15], respectively. The ternary phase diagram of all studied chalcogenide glasses is shown in Fig. 2. Table 1 summarizes all glass compositions studies with corresponding <r> values. Binary stoichiometric compositions occur for $As_{40}S_{60}$, $As_{40}Se_{60}$, and $Ge_{33}Se_{67}$ with <r> of 2.40, 2.40, and 2.66, respectively.

As-S Raman spectra were measured using an alpha300 RA (WITec GmbH, Ulm, Germany) confocal Raman microscope. Spectra were collected using a 633 nm excitation wavelength laser with a power of ≈0.5 mW, 1800 g/mm diffraction grating, × 50 magnification objective, and average of 20 accumulations of 20 s integration time. The remaining Raman spectra, including vitreous Se, As-Se, Ge-Se, Ge-As-Se, and commercial Ge-As-Se glasses, were measured using an alpha300R (WITec GmbH, Ulm, Germany) confocal Raman microscope equipped with a 785 nm excitation wavelength laser and tuned to a power between ≈100 μW to 1 mW. Spectra were collected with an integration

[1] Certain commercial equipment or materials are identified in this paper to adequately specify the experimental procedures. In no case does the identification imply recommendation or endorsement by NIST, nor does it imply that the materials or equipment identified are necessarily the best available for the purpose.

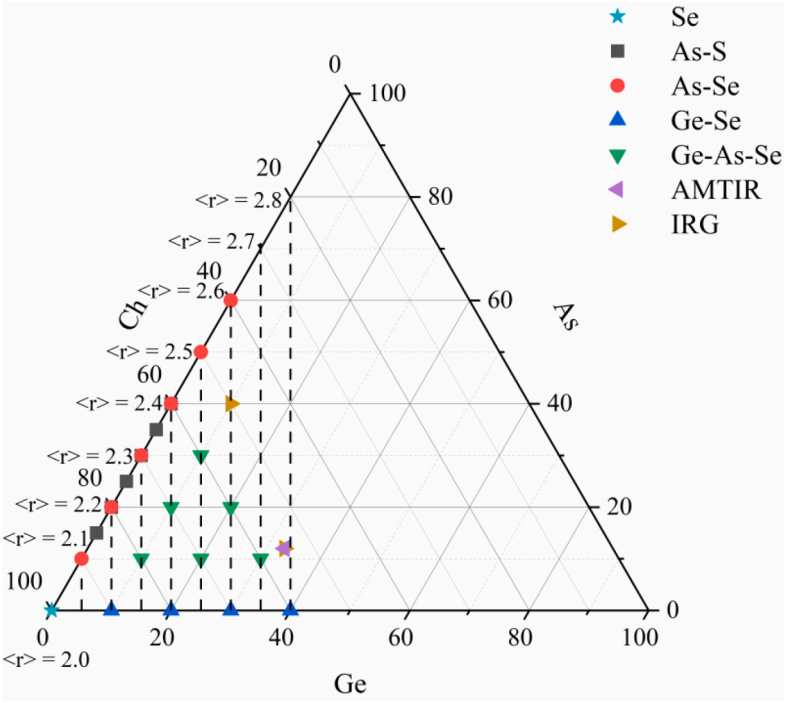

Fig. 2. Ternary diagram of all studied chalcogenide glasses, where vertical lines represent <r>.

time of 10 s and average of 10 accumulations or an integration time of 2 s and average of 100 accumulations were used. Measured spectra were minimally processed by performing cosmic ray removal, bringing each overall spectrum down to a minimum intensity of zero, and performing maximum peak intensity normalization.

A commercial Teraview TPS Spectra 3000 (Teraview, Cambridge, UK) was used for THz-TDS characterization at Alfred University (AU). Real and imaginary optical and dielectric constants were collected from 0.2 to 1.0 THz (composition dependent) in transmission configuration in pure nitrogen. THz radiation was generated using a mode-locked Ti: Sapphire laser operating with a repetition rate of 80 MHz, central wavelength of 800 nm, and pulse duration of 100 fs. Each sample was scanned at five different locations and averaged, resulting in standard deviation in measurements. 3000 scans were collected for each THz spectra with a 1.2 cm^{-1} resolution and 30 scan frequency.

Time-resolved THz-TDS measurements were carried out at NIST following previous experiments seen elsewhere [46–48]. The THz-TDS apparatus is based on a 1 kHz Ti:Sapphire amplifier optical pump-THz probe spectrometer. The apparatus was used to measure THz refractive indices from 0.2 to 1.0 THz operating in transmission mode and to perform kHz low-repetition rate laser irradiation of As-S and As-Se glasses. Probe pulses were blocked with an optical chopper and probe-gate optical delay swept using a translation stage. THz probe was focused using parabolic mirrors to a spot size with a diameter of ≈1.5 mm. Spot laser irradiation was carried out with approximate conditions at a repetition rate of 1 kHz, average beam power of ≈70 mW, pulse duration of ≈40 fs, beam wavelength of 800 nm, beam diameter of ≈3 mm, and for a ≈5 min duration.

3. Results and discussion

3.1. Raman spectroscopy

3.1.1. Unary-vitreous Se bands and glass structure

Fig. 3 shows the Raman spectrum of vitreous selenium, containing bands at ca. 109, 130, 238, 250, and 260 cm^{-1}. The low-frequency bands at ca. 109 and 130 cm^{-1} are characteristic to bond-bending vibrations of

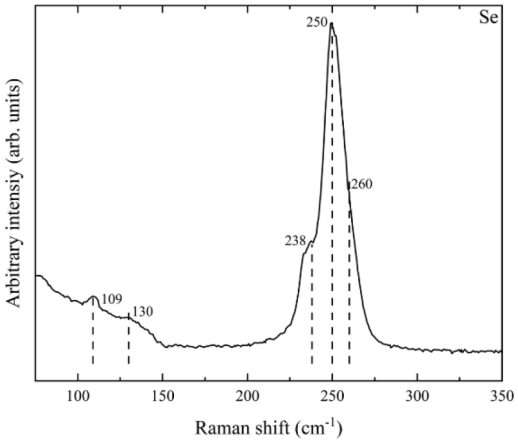

Fig. 3. Maximum intensity arbitrary Raman spectrum of vitreous Se.

selenium units [49–52]. Vitreous selenium has a dominant band at ca. 250 cm^{-1} attributed to selenium chains and rings [49–53]. The low- and high-frequency shoulders of this primary signature are located at ca. 238 and 260 cm^{-1}, and are assigned to vibrational mode of selenium chains [49–53] and rings [49–53], respectively.

Vitreous selenium is defined as having a 0- or 1-dimensional glass network, where selenium atoms are found in chains or rings. Se atoms found in chains and rings are covalently bonded, while van der Waals forces are seen between structural units. Structural and property studies on vitreous selenium can be found elsewhere [7,54]. Experimental Raman spectra indicate that selenium atoms are found chain and ring structural units as the high-frequency band at ca. 250 cm^{-1} dominates the Raman spectra. The low- and high-frequency shoulders reflect selenium found in chains and rings, respectively. The low-frequency vibrational modes suggest bond-stretching vibrations within ring and chain structural units.

3.1.2. Binary – As-S, As-Se, and Ge-Se bands and glass structures

Experimental Raman spectra for binary arsenic sulfide (As-S), arsenic selenide (As-Se), and germanium selenide (Ge-Se) glasses are shown in Fig. 4 (a), (b), and (c), respectively. Raman spectral changes including band and intensity evolution is observed with addition of arsenic or germanium to the glass network across the experimental compositional space, ultimately suggesting structural changes with progression of a glass system. Table 2 summarizes experimental Raman band positions, assignment of bands, and corresponding literature references for binary chalcogenide glasses.

Increasing arsenic content in favor of sulfur, $As_{15}S_{85}$ (<r> = 2.15) to $As_{40}S_{60}$ (<r> = 2.40), reflects the polymerization and increased connectivity of the glass network as observed from the Raman spectra. That is, a S-rich glass such as $As_{15}S_{85}$ consists of excess sulfur found in rings or chains as observed from the bending and stretching modes at ca. 152, 219, 236, 463, 473, and 493 cm^{-1}. Within the spectral envelope, found at ca. 300 to 400 cm^{-1}, are two bands at ca. 335 and 361 cm^{-1}. These bands are attributed to asymmetric and symmetric stretching modes of $AsS_{3/2}$ pyramids, respectively. This envelope reflects the role arsenic plays in the glass network, forming arsenic structural units. Where the excess sulfur can be found in chains or rings. Further introduction of arsenic results in spectral changes culminating to the $As_{40}S_{60}$ spectra. Raman spectral changes suggest shortening sulfur chains and removal of sulfur rings, as sulfur is used to create $AsS_{3/2}$ pyramidal structure units, seen at ca. 340 cm^{-1}. Such $AsS_{3/2}$ pyramidal units increase the glass connectivity. Low intensity bands at ca. 187, 234, and 493 cm^{-1} are due to numerous structural units including bending modes of $AsS_{3/2}$ pyramids and stretching vibrations of sulfur rings or chains. It is suggested at this stoichiometric glass composition that reduced quantities of excess sulfur are found in chains, due to the low intensity. Such Raman spectral changes suggest the transformation of a glass network of $As_{15}S_{85}$ consisting of sulfur rings and chains, with few $AsS_{3/2}$ pyramids cross linking the longer sulfur chains, into the stoichiometric composition of $As_{40}S_{60}$ with a 2- or 3-D glass network consisting of $AsS_{3/2}$ pyramids with reduced quantities of, if any, shorter sulfur chains, representing the excess sulfur not used in creation of $AsS_{3/2}$ pyramids, ultimately forming sheets or layers. Low-repetition rate femtosecond laser irradiated As-S Raman spectra (seen in red in Fig. 4 (a)) show nearly identical spectral signatures as pristine glass, suggesting minimal structural changes observable by Raman spectroscopy. Minimal spectral changes go against literature that demonstrates formation of wrong bonds, e.g., As-As or S-S, while we observe reversible photodarkening with time.

Gradual substitution of arsenic content in place of selenium, $As_{10}Se_{90}$ (<r> = 2.10) to $As_{40}Se_{60}$ (<r> = 2.4), results in polymerization and increased connectivity of the glass network observed through gradual shifts in the Raman spectra, concluding with a reduced dimensionality and connectivity with further transformation to $As_{60}Se_{40}$ (<r> = 2.6) [75]. A Se-rich glass primarily consists of selenium chains or rings, described by the asymmetric band at ca. 251 cm^{-1}. The low frequency shoulder associated with this band at ca. 223 cm^{-1} reflects the role of the reduced arsenic content plays in the glass structure, through initial formation of $AsSe_{3/2}$ pyramidal structural units. $AsSe_{3/2}$ pyramids connect the selenium chains and increased the dimensionality/connectivity of the glass. Further addition of arsenic in place of selenium results in further Raman spectral changes, where the low frequency shoulder at ca. 223 cm^{-1} becomes the primary band of the spectra, as seen with $As_{40}Se_{60}$. The previous high intensity band at ca. 251 cm^{-1} shifts to becoming a shoulder associated with the new band. These Raman spectral changes suggest the transformation and further introduction of $AsSe_{3/2}$ pyramids into the glass network, shortening and removing the selenium chains and rings, thus increasing the connectivity and dimensionality. Continued replacement of selenium by arsenic reflects a transformation from a Se- to As-rich glass including glass network with reduced dimensionality and connectivity, showing associated Raman spectral changes, including the introduction of new defined bands observed for $As_{60}Se_{40}$. $AsSe_{3/2}$ and As_4Se_4 or As_4Se_3 structural units are attributed to the bands at ca. 202, 223, and 235 cm^{-1}. The low intensity and low frequency bands at ca. 111 and 146 cm^{-1} are due to As-As bonds. While the high frequency bands at ca. 253 and 278 are associated with selenium bridges between $AsSe_{3/2}$ pyramids and As_4Se_4 or As_4Se_3 cages. The low intensity bands are associated with selenium chains, while high intensity bands representing the arsenic structural units suggest that selenium is used in forming such units. It is suspected bands associated with selenium at high arsenic content can be explained

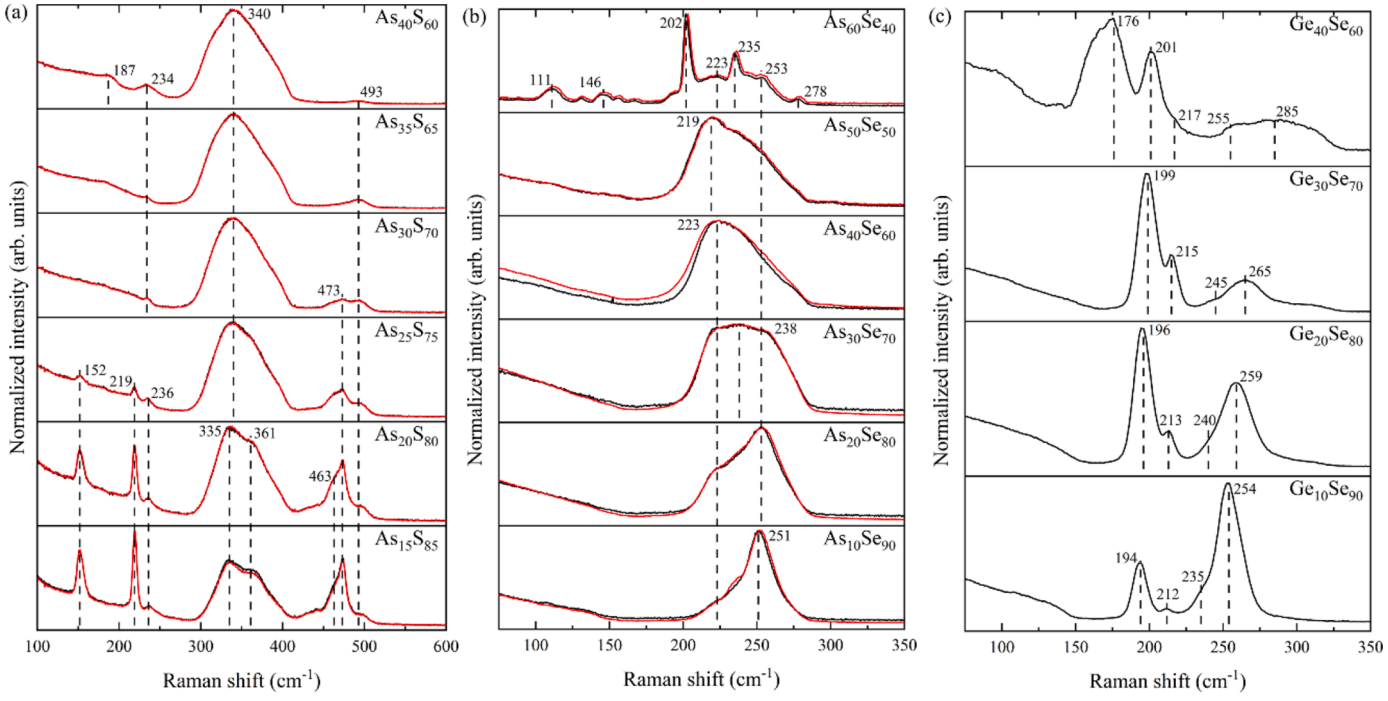

Fig. 4. Maximum intensity normalized Raman spectra of (a) As-S, (b) As-Se, and (c) Ge-Se glasses, black and red correspond to pristine and laser irradiated Raman spectra, respectively.

Table 2
Raman band positions, assignments, and references appliable to chalcogenide glasses.

Band position at ca. (cm^{-1})	System and Region	Assignment	Refs.
109 to 177	Se As-Se (As-rich) Ge-As-Se	Vibrations of As-As, Ge-As, Ge-Ge bonds within larger structural units and bending modes of Se	[49–51, 55–58]
152	As-S (S-rich)	S-S bending modes and S rings	[59–63]
176	Ge-Se (Ge-rich)	Vibrations of metal-metal or Ge-Ge homopolar bonds	[55]
187	As-S (stoichiometric)	As-As bonds and bending modes of $AsS_{3/2}$ pyramids, S chains, and As_4S_4 cages	[59,64–66]
194 to 201 191 to 197	Ge-Se (Ge-rich) Ge-As-Se (Ge-rich)	Breathing modes of corner-shared $GeSe_{4/2}$ tetrahedra	[67–73]
202	As-Se (As-rich)	As_4Se_4 cages	[49–51,74]
212 to 217 201 to 215	Ge-Se (Ge-rich) Ge-As-Se (Ge-rich)	Breathing modes of edge-shared $GeSe_{4/2}$ tetrahedra	[67–73]
219 219 to 223 212 to 228	As-S (S-rich) As-Se (As-rich) Ge-As-Se (As-rich)	S-S bending modes and symmetric vibrations of S rings As-Se stretching modes in $AsSe_{3/2}$ pyramidal structural units	[49–51,53, 59,61–63, 74,75]
234 to 236 235 to 238 236 to 243	As-S As-Se Ge-As-Se	S-S bonds and S rings (S-rich), and bending modes of $AsS_{3/2}$ pyramids, S rings or chains, and As_4S_4 cages (As-rich) As_4Se_3 cages (As-rich) and Se chains or rings (Se-rich)	[49–51,53, 59,60, 64–66,74, 76]
250 251 to 253 235 to 265 254 to 255	Se As-Se (Se-rich) Ge-Se (Se-rich) Ge-As-Se (Se-rich)	Se rings or chains	[49–51,53, 58,69,70, 72–75]
278	As-Se (As-rich)	Se rings and chains/bridges between $AsSe_{3/2}$ pyramids and As_4Se_4 or As_4Se_3 cages	[49–51,74]
285 290 to 302	Ge-Se (Ge-rich) Ge-As-Se (Ge-rich)	Asymmetric stretching of corner-sharing and out-of-phase stretching of edge-sharing of $GeSe_{4/2}$ tetrahedra, convolution of $GeSe_{4/2}$ tetrahedra, Se ring, and chains	[55,67,77]
335	As-S (S-rich)	Asymmetric stretching modes of $AsS_{3/2}$ pyramids	[60,78,79]
340	As-S (As-rich)	Symmetric stretching vibrational modes of $AsS_{3/2}$ pyramids, low and high frequency shoulders attributed to asymmetric stretching modes of $AsS_{3/2}$ pyramids and As-S-As bridges, respectively	[59,60, 64–66,78, 79]
361	As-S (S-rich)	Symmetric stretching modes of $AsS_{3/2}$ pyramids	[78,79]
463	As-S (S-rich)	S-S stretching in S chains or rings	[61,80]
473	As-S (S-rich)	S-S symmetric vibrations, bending modes in S rings or chains, and S-S linkages between $AsS_{3/2}$ pyramids	[59,61, 64–66, 78–81].
493	As-S (S-rich)	Stretching vibrations of S-S bonds in S rings or chains	[59,64–66, 76,81]

in terms of bridges between arsenic structural units, e.g., As-Se-As, as selenium chains should have both reduced size and quantity, if any appear at all. Raman spectral changes suggest the gradual transformation of a Se- to As-rich glass network and structure. Where selenium is initially found in chains connected by few $AsSe_{3/2}$ pyramidal structural units, consisting of a primarily 1-D glass network, into that of a 2- or 3-D glass network consisting of primarily $AsSe_{3/2}$ in sheets or layers, and concluding with reduced dimensionality and connectivity with 0-D As_4Se_4, and As_4Se_3 structural units. Laser irradiated As-Se binary chalcogenide glass Raman spectra (shown in red in Fig. 4 (b)) have minimal observable Raman spectral changes across the binary series, suggesting minimal structural changes are observed through Raman spectroscopy. Raman spectral changes of $As_{10}Se_{90}$ observes a slight intensity discrepancy of the low-frequency shoulder observed at ca. 235 cm^{-1}, where the laser irradiated spectra has an intensity increase of the shoulder, attributed to selenium chains and rings. $As_{60}Se_{40}$ Raman spectral changes are observed at ca. 202 and 235 cm^{-1}, the former shows a upshift in frequency and a slight peak shift change, and the latter shows an upshift in frequency and relative intensity increase. The reduced quantity of slight Raman spectral changes suggests nominal measurable structural changes via Raman spectroscopy. However, reversible, with time, photodarkening was observed for As-Se glasses.

Raman spectral changes of Ge-Se glasses reflect the substitution of germanium content for selenium content, $Ge_{10}Se_{90}$ ($<r> = 2.20$) to the stoichiometric composition of $Ge_{33}Se_{67}$ ($<r> = 2.66$, this composition is not studied in this series) to $Ge_{40}Se_{60}$ ($<r> = 2.80$), seen with an initial increase and subsequent reduction in connectivity and dimensionality, e.g., polymerization followed by depolymerization, of the glass network. Germanium is found in four-fold coordination as $GeSe_{4/2}$ structural units, with selenium in ring and chain structural units. Se-rich Ge-Se glass Raman spectra are dominated by populations of selenium rings or chains through the band at ca. 254 cm^{-1}. $GeSe_{4/2}$ tetrahedra structural units are found in reduced quantities in corner- and edge-sharing configurations, observed at ca. 194 and 212 cm^{-1}, respectively. Increased quantities of germanium, and reduction of selenium content, is seen through increased band intensities of corner- and edge-sharing $GeSe_{4/2}$ tetrahedra. $GeSe_{4/2}$ tetrahedra become the dominant structural units, as selenium chains show a reduction in population through relative intensity reductions. Relative band intensities of corner- and edge-shared $GeSe_{4/2}$ tetrahedra allow for differentiation as to which species is dominant and makes up the glass network. Ge-Se glasses have $GeSe_{4/2}$ tetrahedra primarily in corner-sharing $GeSe_{4/2}$ configuration, with reduced quantities of edge-sharing $GeSe_{4/2}$ configurations, observed through relative band intensity ratio. Increased germanium content shows a general upshift of all band positions. Ge-rich, or Se-deficient, Ge-Se glasses beyond the stoichiometric composition of $Ge_{33}Se_{67}$ have the most pronounced spectral changes through development of bands at ca. 176 and 285 cm^{-1}. The former is characteristic to Ge-Ge homopolar bonds and the latter to vibrational modes of $GeSe_{4/2}$ tetrahedra. We suspect the band centered at ca. 201 cm^{-1} with a shoulder at ca. 217 cm^{-1} is a convoluted band attributed to both edge-sharing and corner-sharing $GeSe_{4/2}$ tetrahedra seen at increased Ge content. Ge-rich Ge-Se glasses have increased quantities of $GeSe_{4/2}$ tetrahedra with reduced populations of, if any, selenium chains. However, at $Ge_{40}Se_{60}$, and even

at $Ge_{30}Se_{70}$, we suspect that the transformation of $GeSe_{4/2}$ tetrahedra into $GeSe_{3/2}$ tetrahedra with a Ge-Ge bond must occur. Ge-Ge bonds are observed in great quantities as $GeSe_{3/2}$ populations increase, it is suspected selenium atoms are deficient in the ability to satisfy tetrahedral coordination of Ge atoms, resulting in formation of homopolar Ge-Ge bonds. Formation of Ge-Ge homopolar bonds corresponds to a reduced dimensionality, converting the glass network and structural unit into a 1-dimensional ethane-like $(Ch_3)Ge\text{-}Ge(Ch_3)$ unit. Occurrence of these ethane-like $(Ch_3)Ge\text{-}Ge(Ch_3)$ units confirms $GeSe_{3/2}$ is the only unit allowed.

3.1.3. Ternary – Ge-As-Se bands and glass structure

Fig. 5 (a) and (b) shows experimental Raman spectra of ternary germanium arsenic selenide (Ge-As-Se) chalcogenide glasses and commercially available AMTIR 1 ($Ge_{33}As_{12}Se_{55}$), IRG 22 ($Ge_{33}As_{12}Se_{55}$), and IRG 24 ($Ge_{10}As_{40}Se_{50}$) glasses, respectively. Ge-As-Se glass structure is composed of structural units found in As-Se and Ge-Se glasses with arsenic and germanium are found in three- and four-fold coordination, respectively, e.g., $AsSe_{3/2}$ pyramids and $GeSe_{4/2}$ tetrahedra connected via Se chains of varying lengths, identifiable via Raman spectra. Band positions between experimentally and commercially produced Ge-As-Se glasses share vibrational modes and assignments, ultimately dependent upon glass composition. Arsenic and germanium structural units add to the complexity in identifying and assigning bands to any one mode, resulting in convolved bands. Table 2 contains band positions, assignment, and literature references for Ge-As-Se glasses. Raman spectroscopy of commercially available Ge-As-Se glasses have been reported elsewhere [57,77].

Increasing arsenic and germanium content, at the expense of selenium content, serves to cross link the glass network, observed through gradual increase in the average coordination number, <r>. $AsSe_{3/2}$ pyramids and $GeSe_{4/2}$ tetrahedra structural units connect the glass structure, polymerizing the glass structure, and shorten selenium chains found between such units. Understanding Ge-As-Se glasses is carried out through individual examination of the iso-germanium, iso-arsenic, or iso-selenium tie-lines to enhance observed trends in composition and structure.

Examination of the iso-arsenic tie-line Raman spectra shows gradual increased quantities and population of germanium structural units, specifically $GeSe_{4/2}$ tetrahedra, from $Ge_{10}As_{10}Se_{80}$ (<r> = 2.30) to $Ge_{20}As_{10}Se_{70}$ (<r> = 2.50) to $Ge_{30}As_{10}Se_{60}$ (<r> = 2.70). Evolution of the iso-arsenic tie-line shows Raman signatures from corner- and edge-shared $GeSe_{4/2}$ tetrahedra, $AsSe_{3/2}$ pyramids, and selenium chains or rings. Corner- and edge-shared $GeSe_{4/2}$ tetrahedra are observed as the primary Raman bands at ca. 191 and 201 cm^{-1}, respectively. $GeSe_{4/2}$ tetrahedra become the primary structural unit observed in the glass structure, with $AsSe_{3/2}$ pyramids or As_4Se_3 cages in slightly elevated quantities at ca. 214 and 243 cm^{-1}, respectively, and reduced population and sizes of selenium rings and chains connecting such structural units, seen at ca. 255. Ge-Ge homopolar bonds between $GeSe_{3/2}$ tetrahedra are observed in Ge-rich compositions at ca. 177 cm^{-1}.

The iso-germanium tie-line Raman spectra shows increased quantities of arsenic structural units, seen as $AsSe_3$ pyramids, from $Ge_{10}As_{10}Se_{80}$ (<r> = 2.30) to $Ge_{10}As_{20}Se_{70}$ (<r> = 2.40) to $Ge_{10}As_{30}Se_{60}$ (<r> = 2.50). Raman spectral changes of the iso-germanium tie-line shows initial $GeSe_{4/2}$ tetrahedra, $AsSe_{3/2}$ pyramids, and selenium chains or rings. $AsSe_{3/2}$ pyramids and As_4Se_3 cages are the primary structural units found in the glass structure and quantities increase with increasing arsenic content at ca. 214 and 228 cm^{-1}. Selenium chains and rings, at ca. 255 cm^{-1}, show a reduction in population observed through Raman spectra. Corner- and edge-shared $GeSe_{4/2}$ tetrahedra are observed in the glass structure, at reduced quantities compared to arsenic structural units, at ca. 197 cm^{-1}.

Iso-selenium tie-lines of Se = 70 and 60 % allow for examination of glass structure, with $Ge_{10}As_{20}Se_{70}$ (<r> = 2.40) to $Ge_{20}As_{10}Se_{70}$ (<r> = 2.50) or $Ge_{10}As_{30}Se_{60}$ (<r> = 2.50) to $Ge_{20}As_{20}Se_{60}$ (<r> = 2.60) to $Ge_{30}As_{10}Se_{60}$ (<r> = 2.70), respectively. Raman spectra of Ge-As-Se glasses with Se =70 % have either increased quantities of germanium or arsenic with higher populations of $GeSe_{4/2}$ tetrahedra or increased $AsSe_{3/2}$ pyramids and As_4Se_3 cages, respectively. At Se = 60 % Raman spectra show Ge-rich, As-rich, and equal Ge and As content, with spectral changes reflecting composition and population of structural units. It

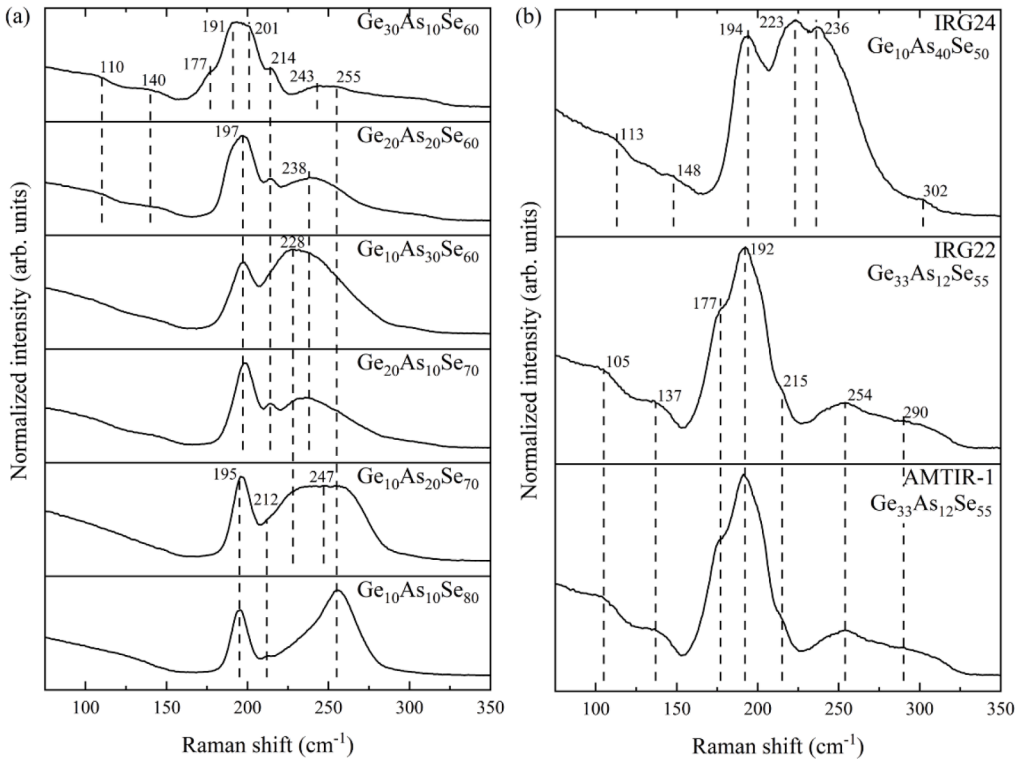

Fig. 5. Maximum intensity normalized Raman spectra of (a) experimental and (b) commercial Ge-As-Se glasses.

is important to note for the studied compositions we suspect selenium serves as a bridge between structural units, with reduced quantities and sizes, if any, of selenium chains. Raman spectral changes suggest As-rich Ge-As-Se glasses are composed of arsenic structural units in the form of $AsSe_{3/2}$ pyramids or As_4Se_3 cages found at increased populations, with reduced quantities of $GeSe_{4/2}$ tetrahedra, and selenium chains. Ge-rich Ge-As-Se glass has Raman spectra suggesting $GeSe_{4/2}$ corner- and edge-sharing tetrahedra are the primary structural unit making up most of the glass network, with reduced quantities of $AsSe_{3/2}$ pyramids, As_4Se_3 cages, and selenium chains. Ge-rich glasses show noticeable Ge-Ge bonding between $GeSe_{3/2}$ tetrahedra, as selenium cannot accommodate the four-fold coordinated germanium, seen at ca. 177 cm^{-1}. Equal arsenic and germanium content Ge-As-Se glasses serves as the mid-point between As- and Ge-rich compositions, where $GeSe_{4/2}$ tetrahedra, $AsSe_{3/2}$ pyramids, As_4Se_3 cages, and selenium bridges or, if any, chains are all observed in the Raman spectra in significant quantities at ca. 197, 214, 238, and 255 cm^{-1}, respectively.

Raman spectral signatures from commercial Ge-As-Se glasses, AMTIR-1 and IRG 22 Ge-rich Ge-As-Se ($Ge_{33}As_{12}Se_{55}$), are identical, as they share identical compositions. IRG 24 As-rich Ge-As-Se ($Ge_{10}As_{40}Se_{50}$) glass has a distinct Raman spectrum from the other two commercial and experimental glasses, as this composition has the highest and lowest arsenic and selenium content, respectively. AMTIR-1 and IRG 22 Raman spectra suggest the glass structure is primarily composed of $GeSe_4$ corner-sharing tetrahedra at ca. 192 cm^{-1}. Low- and high-frequency shoulders of this primary band are due to Ge-Ge homopolar bonds and edge-shared $GeSe_{4/2}$ tetrahedra at ca. 177 and 215 cm^{-1}, respectively. Reduced quantities of $AsSe_{3/2}$ pyramids and selenium chains are suggested due to the broad low-intensity band at ca. 254 cm^{-1}. The broad, low-intensity band at ca. 290 cm^{-1} reflects edge-shared $GeSe_{4/2}$ tetrahedra. Meanwhile, IRG 24 Raman spectra suggest $AsSe_{3/2}$ pyramids, As_4Se_3 cages, and corner-shared $GeSe_{4/2}$ tetrahedra are the primary building blocks of the glass network, seen as one convolved band with peaks at ca. 223, 236, and 194 cm^{-1}, respectively. The high-frequency shoulder at ca. 250 cm^{-1} is due to selenium chains in reduced quantities and sizes, serving to connect the germanium and arsenic structural units. $GeSe_{4/2}$ tetrahedra is supported through the band at ca. 302 cm^{-1}.

3.2. THz-TDS refractive indices

It is common knowledge that glass structure dictates the resulting properties. This holds true for THz optical properties as well. THz properties, specifically the refractive index, have been recently reviewed for chalcogenide glasses, among other glass families, by Sundaram [82], along with individual studies carried out for selective compositions. Sundaram et al. [83] examined the binary As-S glass system using a THz spectrometer for transmission measurements. Results reflect compositional dependence of the refractive index allowing for compositional control over THz properties. Between 30 to 40 at.% As increases the refractive index values at 0.2 THz, beyond 40 at.% results in a reduced refractive index, associated with structural changes. McCloy et al. [18] have measured the refractive index of As_xS_{100-x} glasses, x = 30, 33, 36, 40, and 42 at.%, at visible, infrared, and sub-millimeter frequencies. Increasing <r> and As content have higher measured refractive index values, reaching a maximum 40 at.% or <r> = 2.4 and further As content results in lower refractive index values. This refractive index trend is universal to all measured frequencies, due to connectivity between atoms and structural changes across the compositional space. As previously stated, <r> = 2.4 is associated with an ideally connected glass network that is optimally-constrained. This study concludes that a more compact structure, with <r> = 2.4, has a minimum V_m and maximum refractive index at all studied frequencies for binary As-S and As-Se series. Kang et al. [84] and Ravagli et al. [85] both reviewed optic and dielectric constants of more complex chalcogenide systems at THz frequencies, with a focus on refractive index and absorption coefficient values.

Chalcogenide glasses have been selectively varied across the compositional space, resulting in various <r> values and fundamental building block structural units, providing a basis for understanding the connection between the glass structure and resulting THz properties. It is important to note that the structure-THz properties relationship has not been extensively studied for glasses, let alone for the selected chalcogenide glass families and specific compositional spaces at these defined THz frequencies. Sulfur atoms have a smaller polarizability, with more ionic bonding, than selenium atoms resulting in reduced refractive index values for glasses of defined compositions. The average coordination number, <r>, is used to describe the glass structure, connectivity, network, and final properties. In the case of binary chalcogenide glasses of compositions of As_2S_3 and As_2Se_3, the highest THz refractive index corresponds to <r> = 2.4 in their respective glass systems.

Fig. 6 (a) shows the first of its kind of data of refractive index at 1.0 THz as a function of <r>, highlighting intra- and inter-trends within one and between multiple chalcogenide families. 1.0 THz is selected as a frequency of focus for specific THz refractive index and <r> comparison of all chalcogenide glasses, due to the reduced dispersion and role it plays as a midpoint within the larger measured bandwidths for specific glass systems. Glass systems covering a wide bandwidth region have choppy refractive indices, i.e., show the etalon effect, at low THz values, i.e., 0.2 to 0.5 THz, that could be explained due to samples possessing a reduced sample thickness, e.g., less than 1 mm, on the order of the wavelength of THz waves. The oscillation in THz refractive indices, i.e., etalon effect, is observed for vitreous Se, Ge-Se, and Ge-As-Se from 0.2 to 0.75 THz and is due to sample thickness and not due to vibrational behavior of the glass structure at THz frequencies, as glasses do not exhibit absorption bands characteristic to glass structure at THz frequencies, e.g., if the sample thickness was greater than 1 mm then refractive index dispersion would not be observed. Fig. 6 (b) shows the 1.0 THz refractive index in the Ge-As-Se family across the ternary compositional space. The largest THz refractive index is seen for the $As_{40}Se_{60}$ composition and an incremental increase in the 1.0 THz refractive index as Se content is reduced is observed. Fig. 6 (c) presents change in refractive index (Δn) at 1.0 THz refractive index values as a function of <r> in for As-S and As-Se binary chalcogenide glasses due to low-repetition rate femtosecond laser irradiation. The measured Δn and standard deviation for both As-S and As-Se glasses are minimal on the order of 10^{-3} and 10^{-3} to 10^{-4}, respectively. Distinct compositions within both As-S and As-Se series measure relatively higher Δn, as seen in Fig. 6 (c). As-S compositions of $As_{15}S_{85}$ and $As_{25}S_{75}$ have higher Δn of 0.0090 and 0.0054 and standard deviation of 0.0051 and 0.0017, respectively. As-Se compositions of $As_{20}Se_{80}$ and $As_{30}Se_{70}$ record higher Δn of -0.0357 and 0.0282 with standard deviation of 0.0116 and 0.0152, respectively. The refractive index changes are on the order of those reported in literature by Refs. [31,33,44], with Δn between 10^{-2} to 10^{-4} and ultimately dependent upon glass compositions, laser parameters, and wavelength of measurement. Understanding laser irradiated THz refractive index changes will enable writing optical components in glasses of tailored compositions for various THz applications that require specific refractive index values. Our results show laser irradiation could be used on select compositions to provide varying degrees of refractive index changes, i.e., if an application requires minimal changes to a pristine refractive index, then laser irradiation could be implemented to reach the targeted refractive index.

3.2.1. Evaluation of THz refractive index from THz-TDS at Alfred University (AU) and NIST

The accuracy of the THz-TDS system at AU was verified through refractive index measurements at THz frequencies obtained from THz-TDS system at NIST for all As-S and As-Se binary chalcogenide glasses. At AU, each sample was scanned five times and averaged, resulting in standard deviations on the order of 10^{-2} to 10^{-3}. The average AU THz measurement was compared to a single average measurement obtained

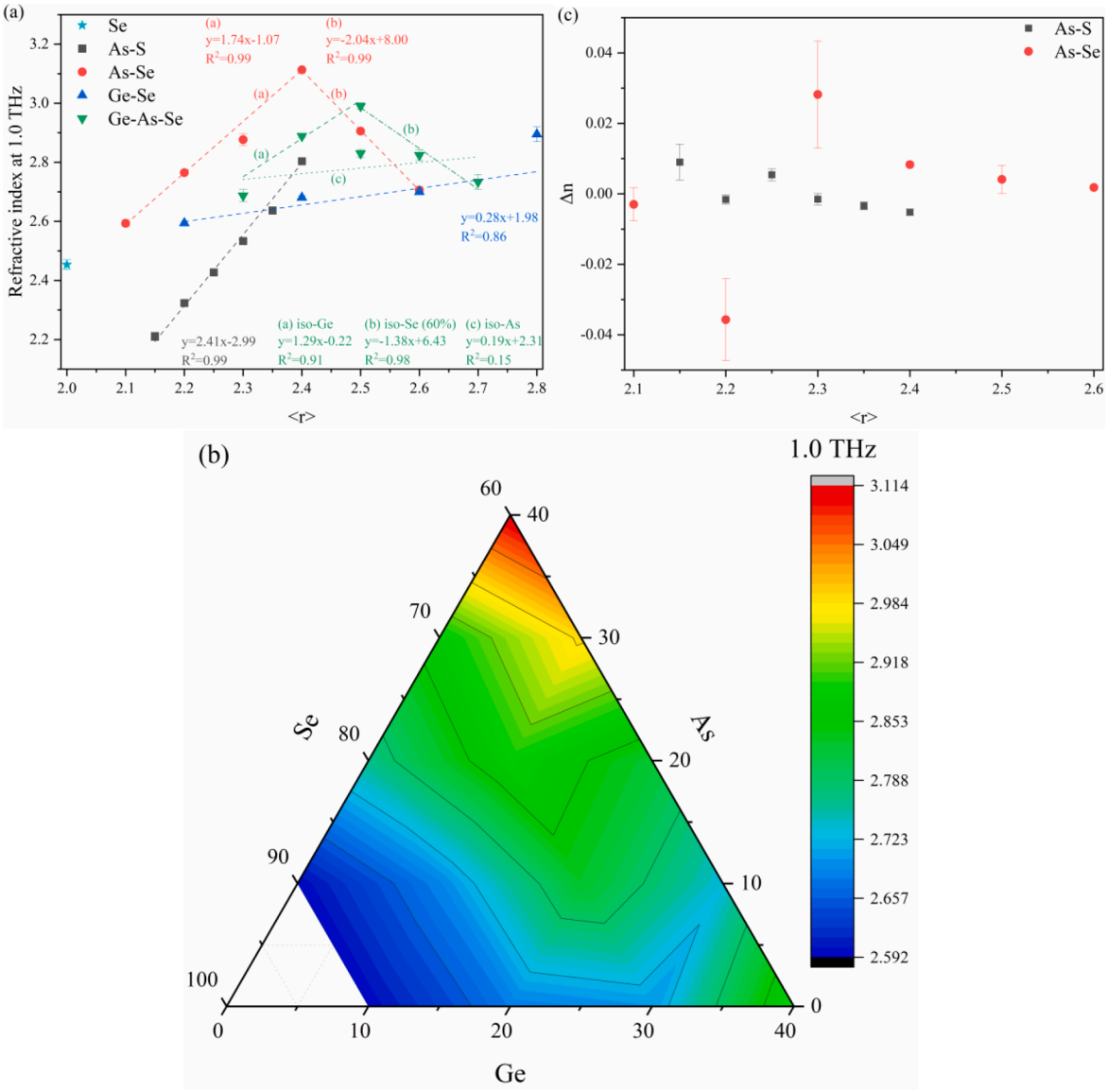

Fig. 6. (a) Se, As-S, As-Se, Ge-Se, and Ge-As-Se pristine 1.0 THz refractive index as a function of <r>, average of five collected spectra and error bars (standard deviation) are included, (b) Ge-As-Se 1.0 THz ternary diagram, and (c) As-S and As-Se change in 1.0 THz refractive index, Δn, due to femtosecond laser irradiation as a function of <r>.

from NIST. The percent error (δ) between the two instruments was less than 1 %, except laser irradiated $As_{20}Se_{80}$ with 1.61 %. $As_{40}S_{60}$ and $As_{40}Se_{60}$, presented due to both compositions possessing <r> = 2.4 and being the most well-known and studied compositions within the two binary series, refractive index as a function of frequency between 0.2 and 1.0 THz obtained at AU and NIST is shown in Fig. 7 (a). Average THz refractive index measurements from 0.2 to 1.0 THz measured at both AU and NIST are remarkably accurate with pristine $As_{40}S_{60}$ and $As_{40}Se_{60}$ having a percent error (δ) of 0.19 % and 0.03 %, respectively. Laser irradiated $As_{40}S_{60}$ and $As_{40}Se_{60}$ have a percent error of 0.41 % and 0.27 %, respectively. AU and NIST average refractive index values are over 0.2 to 1.0 THz and percent error (δ), calculated using $\delta = (|NIST - AU|/AU) \times 100$, of each binary composition was calculated and shown in Fig. 7 (b). Pristine percent error is generally less than the laser irradiated percent error for both As-S and As-Se glass series. The As-S pristine and laser irradiated δ is between 0.02 to 0.70 % and 0.16 to 0.69 %, respectively, while the As-Se pristine and laser irritated δ is between 0.01 to 0.27 % and 0.03 to 1.61 %, respectively. The percent error associated with THz refractive index measurements confirms the accuracy and places great confidence in THz-TDS refractive index measurements taken at AU of high optical quality produced samples. Our THz refractive index measurements at AU and NIST show the measured error is within the error of the instrument(s).

3.2.2. *Unary-vitreous Se*

The THz refractive indices of vitreous selenium over 0.2 to 2.5 THz are shown in Fig. 8. Vitreous Se is defined as having a 0- or 1-dimensional glass network with selenium atoms found in chains or rings, with <r> = 2.0. As expected, the measured n(THz) is the lowest of all Se containing glasses, where addition of additional elements, e.g., As or Ge, increase the connectivity and dimensionality of the glass network and <r>. Vitreous Se n(THz) falls in line with the measured n(THz) of As-Se and Ge-Se series and follows the trendlines for both series, ultimately serving as the minimum of both. In the As-Se series the <r> increases by 0.1 for every As addition and the Ge-Se has increases in <r> by 0.2.

3.2.3. *Binary-As-S, As-Se, and Ge-Se*

Fig. 9 (a)–(c) show the refractive index from 0.2 to 1.0 and 0.2 to 2.0 THz of binary As-S, As-Se, and Ge-Se chalcogenide glasses, respectively.

Within the As-S binary series a polymerized glass network and

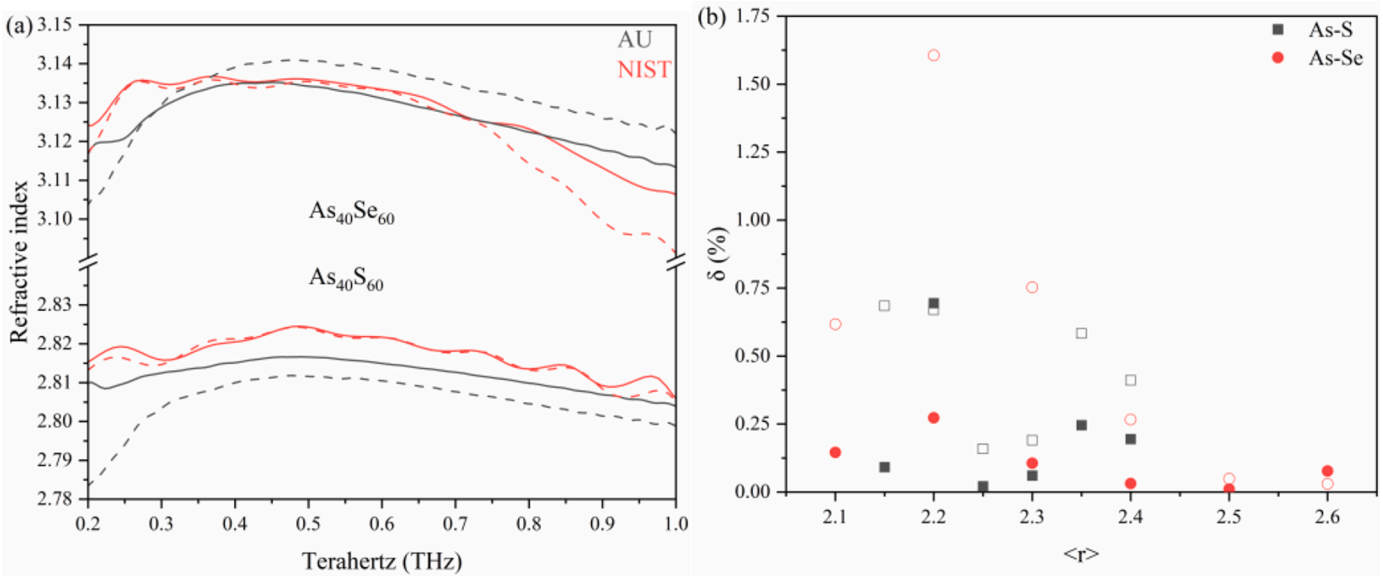

Fig. 7. (a) Refractive index of pristine (solid) and laser irradiated (dashed) $As_{40}S_{60}$ and $As_{40}Se_{60}$ from 0.2 to 1.0 THz measured at AU (black) and NIST (red) and (b) percent error for n(THz) of pristine (solid) and laser irradiated (hollow) As-S (black) and As-Se (red) glasses as a function of composition <r>.

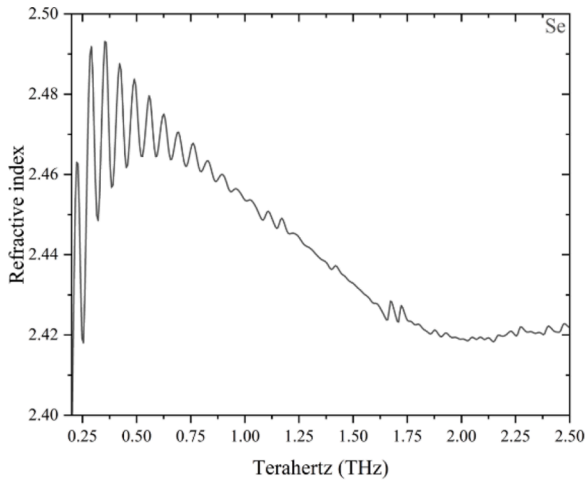

Fig. 8. Vitreous Se refractive index from 0.2 to 2.0 THz, average of five collected spectra. Oscillations below 1.0 THz arise from the etalon effect as previously discussed.

increased connectivity, described by <r>, consisting of $AsS_{3/2}$ pyramids, among other structural units, exhibits a larger terahertz refractive index within the THz regime. A clear increasing linear relationship at 1.0 THz refractive index as a function of <r>, and increasing arsenic content via substitution with sulfur content, is seen in Fig. 6 (a). Raman spectroscopy suggests further increasing arsenic content results in shortening of sulfur chains and increased crosslinking through $AsS_{3/2}$ pyramidal structural units, this trend and increased dimensionality occurs up to the stoichiometric composition of $As_{40}S_{60}$ that is composed of $AsS_{3/2}$ pyramids forming layers or sheets with minimal, if any, sulfur chains. The $AsS_{3/2}$ pyramidal units are responsible for the increased connectivity and <r>, ultimately leading to an increased THz refractive index value. Arsenic itself has a larger polarizability than sulfur, supporting the premise of increasing THz refractive index values with increasing arsenic content. The maximum 1.0 THz refractive index value of studied As-S glasses occurs for $As_{40}S_{60}$, which has an <r> = 2.4 and optimally constrained network. The pristine and laser irradiated refractive index trend observed at 1.0 THz continues throughout the THz regime from 0.2 up to 1.0 THz, visible in Fig. 9 (a). This experimental THz refractive index data supports the premise that the refractive index is at a maximum for arsenic sulfide glasses with <r> = 2.4, occurring at $As_{40}S_{60}$. Laser irradiated regions of As-Se glasses have minimal measurable THz refractive indices changes, with $As_{15}S_{85}$ and $As_{25}S_{75}$ showing the largest laser induced refractive index changes, suggesting

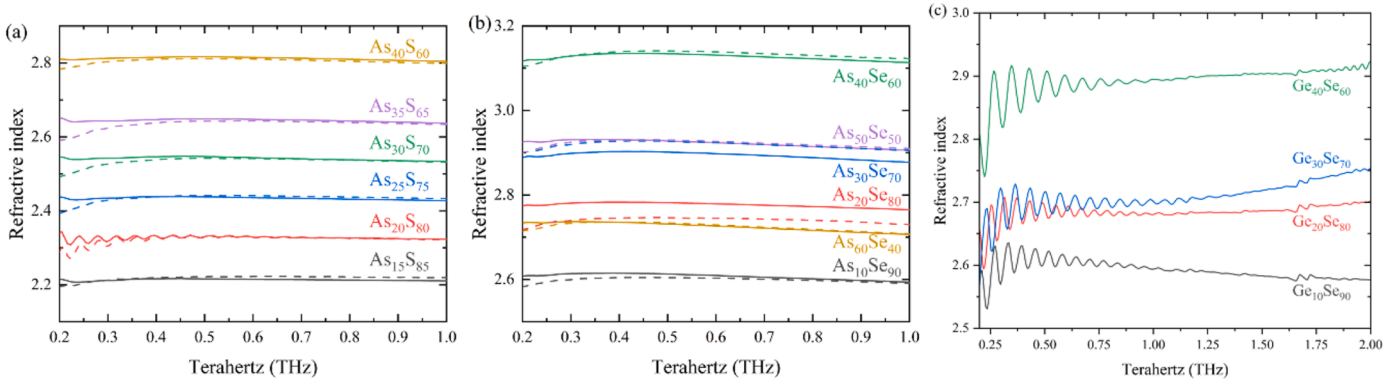

Fig. 9. (a) As-S, (b) As-Se, and (c) Ge-Se series refractive index from 0.2 to 1.0 or 0.2 to 2.0 THz, average of five collected spectra, pristine and laser irradiated spectra are solid and dashed lines, respectively. In (c) oscillations below 1.0 THz arise from the etalon effect as previously discussed.

studied laser conditions have little to no impact on the structure and THz refractive indices. Photodarkening was observed for all As-S glasses due to laser irradiation, that was for the most part, reversed qualitatively back to the original state with time.

Observed 1.0 THz refractive index values reflect structural and polymerization changes from a Se- to As-rich glass network, supported by the Raman spectra data. Refractive index values see an initial increase as polymerization of the glass network occurs up until the stoichiometric composition and subsequent reduction with further depolymerization as <r> increases. Where addition of arsenic results in formation of $AsSe_{3/2}$ pyramidal units, among other structural units, connecting the glass network and shortening selenium chains. The arsenic selenide glasses have a maximum THz refractive index value occurring for the stoichiometric composition of $As_{40}Se_{60}$ with <r> = 2.4, which is defined as an optimally constrained network. The low and high <r> sides represent Se- and As-rich glass networks with under- and over-constrained networks, respectively, and are associated with changes in refractive index values, found in Fig. 6 (a). Where the Se-rich glass network consists of long selenium chains cross linked by the few $AsSe_{3/2}$ pyramids. At the stoichiometric composition of $As_{40}Se_{60}$ the glass network is composed of $AsSe_{3/2}$ pyramids forming layers or sheets, with reduced quantities, if any, of selenium chains. Further introduction of arsenic beyond $As_{40}Se_{60}$ reflects an As-rich glass network, consisting of questionable quantities, if any, of reduced/shortened selenium chains cross linked by $AsSe_{3/2}$ pyramids. The glass network is dominated by As_4Se_4 and As_4Se_3 cages, with increased As-As linkages and reduced dimensionality and connectivity results in a decreased THz refractive index. The 1.0 THz pristine and laser irradiated refractive index trend is consistent throughout the THz regime from 0.2 to 1.0 THz, as seen in Fig. 9 (b). As-Se experimental data supports the previously discussed maximum THz refractive index values occurring for <r> = 2.4. Vitreous Se falls in line with the measured As-Se THz refractive indices, serving as the minimum of the binary series. It is suspected that vitreous Se would follow this trend, as introduction of As results in conversion into the binary series. Irradiated As-Se glasses measure slight changes in measurable THz refractive indices changes, with $As_{20}Se_{80}$ and $As_{30}Se_{70}$ measuring the highest laser induced refractive index changes, confirming studied laser conditions have minimal structure and THz property changes. As-Se glasses showed the same reversible photodarkening effects with time, as those observed in As-S glasses, due to laser exposure.

Ge-Se binary glasses have observable Raman spectral changes as germanium content replaces selenium content, suggesting initial polymerization, e.g., increased dimensionality and connectivity, of the glass network from $Ge_{10}Se_{90}$ up until the stoichiometric composition of $Ge_{33}Se_{67}$, beyond this the glass networks reflect a reduction in dimensionality and connectivity for the $Ge_{40}Se_{60}$ composition. Structural changes are due to increased populations of four-fold coordinated $GeSe_{4/2}$ tetrahedra that shorten selenium chains. Beyond the stoichiometric composition formation of 1-dimensional ethane-like (Ch_3)Ge-Ge (Ch_3) unit occurs, reducing the dimensionality of the glass network, with Ge-Ge homopolar bonds. Increased quantity of $GeSe_{4/2}$ tetrahedra lead to a concurrently higher measurable THz refractive index within the measured bandwidth. Ge-Se compositions have a systematic increase in <r> from 2.2 to 2.8, where the refractive index increases beyond <r> = 2.4. This trend, i.e., increase in THz refractive index beyond <r> = 2.4, is not observed for other binary As-S and As-Se chalcogenide glasses studied, due to the formation of four-fold coordinated $GeSe_{4/2}$ tetrahedra and transformation into $GeSe_{3/2}$ tetrahedra with Ge-Ge homopolar bonds within the ethane-like (Ch_3)Ge-Ge(Ch_3) units at increased Ge content of $Ge_{40}Se_{60}$. $Ge_{40}Se_{60}$ records the maximum refractive index in the THz bandwidth of the studied Ge-Se compositions, possessing an <r> = 2.8 and therefore the highest bonding constraint with an over-constrained network of all studied systems, as reported in Fig. 9 (c). Increased germanium content with $Ge_{40}Se_{60}$ has the largest quantity of $GeSe_{3/2}$ tetrahedra and homopolar Ge-Ge bonds. Interestingly, this increase in THz refractive index with increasing Ge content and <r> is not observed and measured with IR refractive index, where addition of Ge results in lower measurable refractive index values. One explanation for the observed refractive index trends at THz frequencies would be due to the Ge-Ge homopolar bonds and ethane-like units possessing increased ionic contribution to polarizability and therefore refractive index at THz frequencies. THz refractive index of vitreous Se agrees with that of Ge-Se, serving as a minimum when concurrently examined with the binary series.

3.2.4. *Ternary-Ge-As-Se*

Experimentally produced and commercially available Ge-As-Se glass refractive index from 0.2 to 2.0 and 0.2 to 1.5 THz are presented in Fig. 10 (a) and (b), respectively, and 1.0 THz refractive index values trends are shown in Fig. 6 (a). Gradual substitution of Ge or As content in place of Se content results in a gradual increase in <r>, with subsequent further introduction of $GeSe_{4/2}$ and $AsSe_{3/2}$ structure units increase the connectivity and dimensionality, and thus polymerization of the glass network. Higher and subsequent reduction in measurable THz refractive index values are observed for increasing <r> up until and then beyond 2.5, respectively. $Ge_{10}As_{30}Se_{60}$ has the highest measurable terahertz refractive index of the studied Ge-As-Se series. Individual examination of tie-lines allows for elucidation of observed structural and THz trends for ternary Ge-As-Se glasses, including the iso-arsenic, iso-germanium, and iso-selenium tie-lines.

The iso-arsenic tie-line, reflected through the composition evolution of $Ge_{10}As_{10}Se_{80}$ (<r> = 2.3) to $Ge_{20}As_{10}Se_{70}$ (<r> = 2.5) to $Ge_{30}As_{10}Se_{60}$ (<r> = 2.7), has an initial increase and subsequent reduction in measured terahertz refractive index, with a maximum for <r> = 2.5. The maximum n(THz) is observed with an increase in Ge content with subsequent increase in <r> is reflected through formation of additional $GeSe_{4/2}$ tetrahedra and reduced Se chains. $AsSe_{3/2}$ pyramid Raman signal is more easily identifiable with reduced Se chains, with minimal population changes. The reduction beyond <r> = 2.5 can be attributed to homopolar Ge-Ge bonds as Ge content and $GeSe_{3/2}$ tetrahedra populations increase, ultimately resulting in lower measured n (THz) and over-constrained network.

Iso-germanium tie-line, $Ge_{10}As_{10}Se_{80}$ (<r> = 2.30) to $Ge_{10}As_{20}Se_{70}$ (<r> = 2.4) to $Ge_{10}As_{30}Se_{60}$ (<r> = 2.5), has increasing n(THz) with <r>, reaching a maximum at <r> = 2.5. Increased quantities of $AsSe_{3/2}$ pyramids and As_4Se_3 cages is reflected with subsequent increase in n (THz). $GeSe_{4/2}$ tetrahedra have minimal quantity shifts, still observed in the Raman spectra. Meanwhile Se chains show reduced Raman signal, reflecting less quantities of chains. Interestingly, the highest measurable n(THz) does not occur for <r> = 2.4. Instead, the highest n(THz) is seen for the over-constrained network at <r> = 2.5, suggesting reduced quantities of $GeSe_{4/2}$ tetrahedra with absent Ge-Ge homopolar bonds seen in Ge-rich glasses and increased $AsSe_{3/2}$ pyramids promote larger n (THz) values.

Ge-As-Se glass of the iso-selenium tie-line of Se = 70 %, seen with compositional transformation of $Ge_{10}As_{20}Se_{70}$ (<r> = 2.4) to $Ge_{20}As_{10}Se_{70}$ (<r> = 2.5), has a gradual reduction in measurable n (THz). It is suggested through examination of Raman spectra, this n (THz) trend is due to reduction of $AsSe_{3/2}$ pyramids and As_4Se_3 cages with concurrent quantity increase in $GeSe_{4/2}$ tetrahedra. An over-constrained network has a lower n(THz) than an optimally constrained network. Reviewing the Se = 60 % iso-selenium tie line, i.e., $Ge_{10}As_{30}Se_{60}$ (<r> = 2.5) to $Ge_{20}As_{20}Se_{60}$ (<r> = 2.6) to $Ge_{30}As_{10}Se_{60}$ (<r> = 2.7), follows the same trend. Progressive introduction of further Ge in place of As has an overarching reduction in measurable n(THz). Trends observable in Raman spectra provide an explanation. Increased Ge content has identifiable growth in Ge Raman signal including $GeSe_{4/2}$ and $GeSe_{3/2}$ tetrahedra and preferential homopolar Ge-Ge bonding, while reducing quantities of $AsSe_{3/2}$ pyramids and As_4Se_3 cages is ultimately responsible for lower n(THz) values across the tie-line. Continuously increasing <r> suggest an additional over-constrained glass network and bonding constraints placed on the system, supported

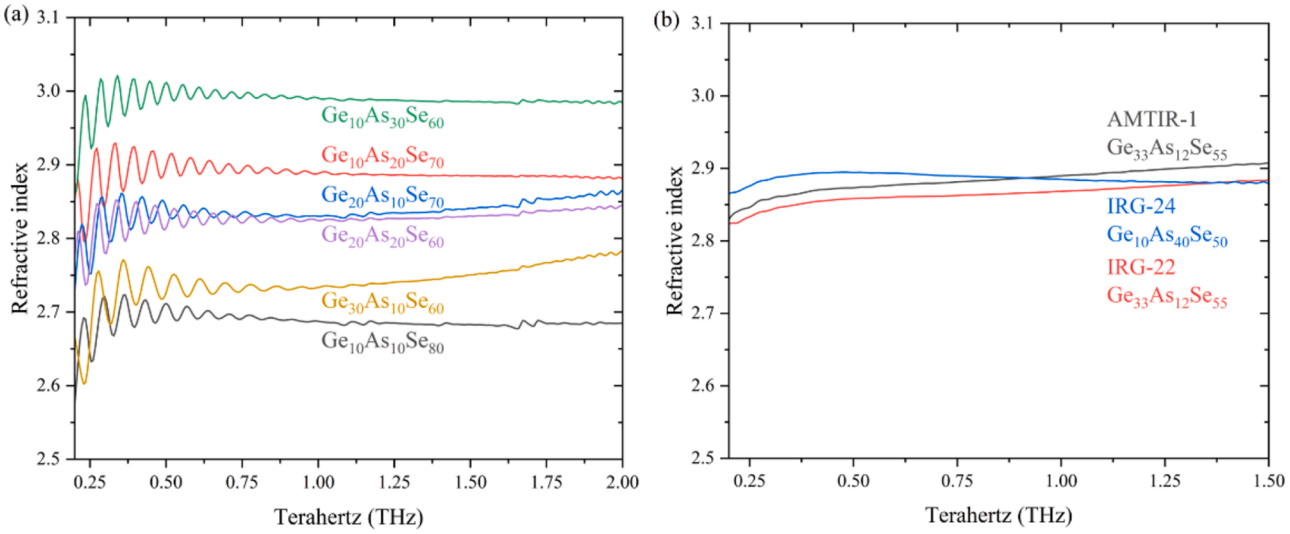

Fig. 10. (a) Experimental and (b) commercial Ge-As-Se series refractive index from 0.2 to 2.0 and 0.2 to 1.5 THz, respectively, average of five collected spectra. In (a) oscillations below 1.0 THz arise from the etalon effect as previously discussed.

through formation of Ge-Ge homopolar bonds, resulting in lower n (THz).

Commercial Ge-As-Se glasses are divided into Ge-rich AMTIR-1 and IRG 22, of the same composition ($Ge_{33}As_{12}Se_{55}$), and As-rich IRG 24 ($Ge_{10}As_{40}Se_{50}$) compositions. Ge-rich glasses Raman spectra reflect increased quantities of $GeSe_{4/2}$ tetrahedra with preferential Ge-Ge homopolar bonds, while containing $AsSe_{3/2}$ pyramids and Se chains in reduced quantities. Reported measured n(THz) values show slight increase with frequency, suggesting measurable dispersion. As-rich glass Raman spectra reflect a glass network consisting primarily of $AsS_{3/2}$ pyramids, As_4Se_3 cages, and $GeSe_{4/2}$ tetrahedra, with reduced Se chains. Measured n(THz) value have a slight decrease with increasing frequency. Both commercially produced Ge-As-Se glasses have minimal dispersion across the measured bandwidth.

3.2.5. LWIR-THz refractive index correlation in As-S, As-Se, Ge-Se, and Ge-As-Se glasses

Specific chalcogenide glass family and larger all-encompassing chalcogenide correlations between the refractive index at IR, e.g., 10 μm, and THz, e.g., 1.0 THz, frequencies allow for estimation of the refractive index at one frequency, if the other is known. Additionally, if structural correlations exist at defined frequency, e.g., structure-THz relationship with refractive index at 1.0 THz, allows for further assumptions and determinations to be made of the refractive index at long-wave infrared frequencies or vice versa. If a chalcogenide glass has a known 1.0 THz refractive index it can be correlated to both glass structure and refractive index at IR frequencies, all of which are critical pieces of information for industrial and consumer applications. Literature reported 10 μm and AU measured 1.0 THz refractive index values are used for this correlation. Fig. 11 (a) shows the long-wave IR-THz refractive index correlation.

Linear IR-THz refractive index correlations are easily identified for As-S, As-Se, and iso-Ge and iso-Se (60 and 70 %) Ge-As-Se glasses. Deviation in linear IR-THz refractive index correlation occurs for both Ge-Se and iso-As Ge-As-Se glasses. Deviation in refractive index correlations is attributed to preferential Ge-Ge homopolar bond found at increased Ge containing glasses with significant quantities of $GeSe_4$ tetrahedra.

Both As-S and As-Se glasses show a clear monotonic increase in THz refractive index with an increase in IR refractive index. Unsurprisingly, the As-Se glasses have a higher measurable THz and IR refractive indices than As-S glasses.

Anomalous behavior seen for Ge-Se glass system in the IR region is observed within the IR-THz refractive index correlation. Below the stoichiometric composition of $Ge_{33}Se_{67}$, Ge-Se glasses show an increase in THz refractive index with reduction in long-wave IR refractive index as Ge content increases from $Ge_{10}Se_{90}$ to $Ge_{20}Se_{80}$ to $Ge_{30}Se_{70}$, suggesting a linear trend. However, above the stoichiometric composition at $Ge_{40}Se_{60}$ the long-wave IR refractive index has a dramatic increase. Interestingly, the THz refractive index increases with Ge content, not following trends observed at IR frequencies. This behavior is attributed to transformation of $GeSe_{4/2}$ into $GeSe_{3/2}$ tetrahedra possessing an increased ionic contribution to the total polarizability at THz frequencies resulting in higher refractive indices as Ge content increases, where this ionic contribution is not active, or contributing, to the total polarizability and refractive indices at IR frequencies, resulting in reduced IR refractive indices when compared to THz refractive indices. Further, it is suggested Ge-Ge homopolar bonds in ethane-like units have an even more significant ionic contribution to the total polarizability and refractive indices, as both IR and THz refractive indices increase beyond the stoichiometric composition with observation of (Ch_3)Ge-Ge (Ch_3) units.

Concurrent examination of the linear trends seen for both the initial Ge-Se glasses below the stoichiometric composition and the As-Se glasses allows for determination of the expected vitreous Se location. The intersections of both trendlines are as expected, ultimately serving as a minimum between the two series. This is confirmed based on THz refractive index information, discussed previously, where vitreous Se serves as the minimum position of both As-Se and Ge-Se glass series with reduced <r>.

Fig. 11 (b) shows the difference between the refractive index, Δn, in the THz and IR regions, n(THz)-n(IR), in the Ge-As-Se family across the ternary space. Difference in refractive index is interpreted to be due to the ionic contribution to the total polarizability, refractive index, and dielectric constant at THz frequencies. Within the ternary diagram the Δn increases with addition of As or Ge content and removal of Se as formation of $AsSe_{3/2}$ pyramids and $GeSe_{4/2}$ tetrahedral structural units occurs, in turn reflecting an increase in <r> and increase in ionic contribution with the presence of higher coordinated structural units. Fig. 11 (c) shows As-S, As-Se, Ge-Se, and Ge-As-Se glass families refractive index difference at THz (0.5 THz) and IR (10 μm) frequencies as a function of <r>. All binary and ternary families studied show a higher Δn with <r>, suggesting formation of $AsCh_{3/2}$ pyramids and $GeSe_{4/2}$ tetrahedra increase the ionic contribution to the refractive index at THz frequencies relative to IR frequencies. Ge-As-Se family of compositions show distinct regions of increased Δn at reduced Se content (60 %) corresponding to significant (30 %) or lack (0 %) of As content.

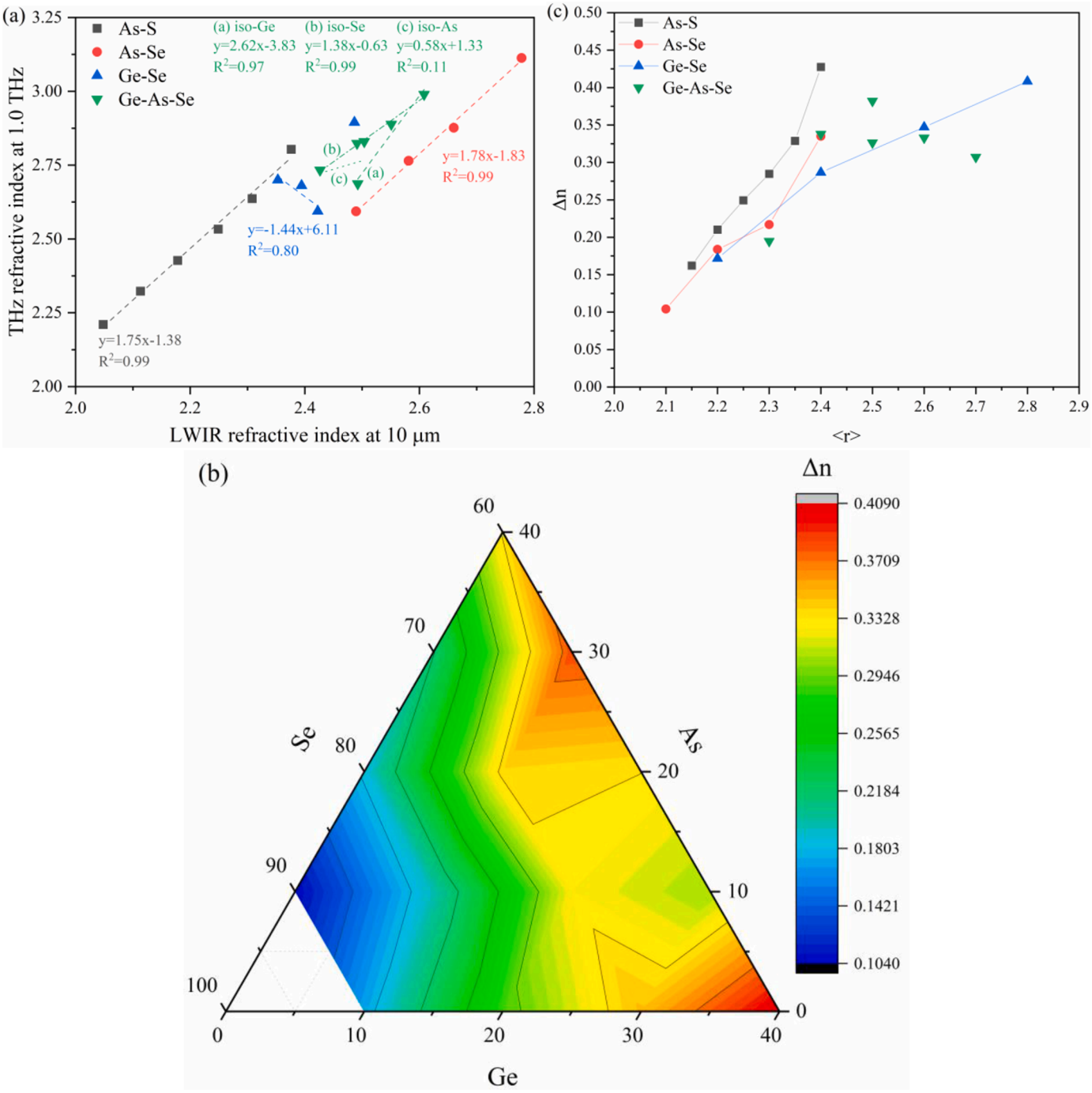

Fig. 11. (a) As-S, As-Se, Ge-Se, and Ge-As-Se LWIR-THz refractive index correlation, (b) Ge-As-Se Δn, $\Delta n = n(THz) - n(IR)$, ternary diagram, and (c) As-S, As-Se, Ge-Se, and Ge-As-Se Δn as a function of <r>.

The significant As containing Ge-As-Se composition of $Ge_{10}As_{30}Se_{60}$ with <r> of 2.5 and binary $Ge_{40}Se_{60}$ (0 % As) with <r> of 2.8 show the highest measured Δn, where $As_{10}Se_{90}$ with <r> of 2.1 measure the lowest Δn. The As-S and As-Se families follows the same trends where $As_{40}S_{60}$ and $As_{40}Se_{60}$ with <r> of 2.4 records the highest Δn of each binary series.

4. Conclusions

Our results support structure-terahertz property relationship within the chalcogenide glass family, where the THz refractive index is ultimately controlled by <r> and, therefore, elemental composition across various chalcogenide glass systems. As-S and As-Se binary glasses have the highest measurable THz refractive index value at <r> = 2.4. Ge-Se binary glasses measure increased THz refractive index as <r> increases, ultimately reaching the maximum for <r> = 2.8. Evaluation of THz-TDS results of As-S and As-Se glasses measured at AU and NIST for both pristine and laser exposed regions match within δ < 1 %, except laser exposed $As_{20}Se_{80}$ which gave a 1.61 % index change. Ternary Ge-As-Se glasses has a maximum measured THz refractive index value at <r> = 2.5, for the $Ge_{10}As_{30}Se_{60}$ composition. Femtosecond laser irradiation of As-S and As-Se glasses at 800 nm with a low-repetition rate resulted in minimal structural and THz refractive index values changes. Long-wave IR-THz refractive index correlations in all studied chalcogenide glasses

show promise for predicting optical properties for integrated THz photonics and potentially dual-mode (LWIR-THz) applications.

Data availability

Data underlying the results presented in this paper are not publicly available at this time but may be obtained from the authors upon reasonable request.

CRediT authorship contribution statement

Nicholas J. Tostanoski: Conceptualization, Methodology, Validation, Investigation, Writing – original draft, Writing – review & editing, Visualization, Project administration. **Edwin J. Heilweil:** Methodology, Validation, Investigation, Writing – review & editing. **Peter F. Wachtel:** Resources, Writing – review & editing, Visualization. **J. David Musgraves:** Resources, Writing – review & editing. **S. K. Sundaram:** Conceptualization, Supervision, Writing – review & editing, Project administration.

Declaration of Competing Interest

The authors declare that they have no known competing financial interests or personal relationships that could have appeared to influence the work reported in this paper.

Data Availability

Data will be made available on request.

Funding

This research did not receive any specific grant from funding agencies in the public, commercial, or not-for-profit sectors.

Acknowledgments

Nicholas Tostanoski acknowledges teaching assistant support from the Inamori School of Engineering. Edwin Heilweil acknowledges internal support from NIST Scientific and Technical Research and Services (STRS) to perform this work. S. K. Sundaram acknowledges support from Kyocera Corporation in the form of Inamori Professorship.

Arsenic sulfide – The Raman instrumentation is based upon work supported by the National Science Foundation under Grant No. DMR-1626164.

Vitreous selenium, arsenic selenide, germanium selenide, and germanium arsenic selenide Raman instrumentation – This work made use of the Cornell Center for Materials Research Shared Facilities supported by the National Science Foundation under Award Number DMR-1719875.

Supplementary materials

Supplementary material associated with this article can be found, in the online version, at doi:10.1016/j.jnoncrysol.2022.122020.

References

[1] J.C. Phillips, Topology of covalent non-crystalline solids I: short-range order in chalcogenide alloys, J. Non Cryst. Solids 34 (1979) 153–181.
[2] M.F. Thorpe, Continuous deformations in random networks, J. Non Cryst. Solids 57 (1983) 355–370.
[3] J.C. Phillips, M. Thorpe, Constraint theory, vector percolation and glass formation, Solid State Commun. 53 (1985) 699–702.
[4] J.C. Mauro, A.K. Varshneya, Multiscale modeling of arsenic selenide glass, J. Non Cryst. Solids 353 (2007) 1226–1231.
[5] A.K. Varshneya, Some comments on physical properties of chalcogenide glasses, J. Non Cryst. Solids 273 (2000) 1–7.
[6] J. Ramsey, G. Lindberg, P. Wachtel, J.D. Musgraves, J. Deegan, Comparison study of a multispectral zoom lens using standard and novel optical materials, Appl. Opt. 58 (2019) 5045–5049.
[7] X.H. Zhang, J.L. Adam, B. Bureau, Chalcogenide glasses. Springer Handbook of Glass, Springer, 2019, pp. 525–552.
[8] S. Sundaram, B.R. Johnson, M.J. Schweiger, J.E. Martinez, B.J. Riley, L.V. Saraf, N. C. Anheier Jr, P.J. Allen, J.F. Schultz, Chalcogenide glasses and structures for quantum sensing. Quantum Sensing and Nanophotonic Devices, International Society for Optics and Photonics, 2004, pp. 234–245.
[9] B. Bureau, X.H. Zhang, F. Smektala, J.L. Adam, J. Troles, H.l. Ma, C. Boussard-Plèdel, J. Lucas, P. Lucas, D. Le Coq, Recent advances in chalcogenide glasses, J. Non Cryst. Solids 345 (2004) 276–283.
[10] M. Hubert, G. Delaizir, J. Monnier, C. Godart, H.L. Ma, X.H. Zhang, L. Calvez, An innovative approach to develop highly performant chalcogenide glasses and glass-ceramics transparent in the infrared range, Opt. Express 19 (2011) 23513–23522.
[11] P.F. Wachtel, A.C. Beckens, J.D. Musgraves, J. Deegan, Refractive index dispersion of germanium-arsenic-selenide (GeAsSe) glasses, Opt. Mater. Express 12 (2022) 1581–1592.
[12] "Amorphous Materials AMTIR-1," in Amorphous Materials Technical Datasheet, (available online).
[13] "Classic-1 Chalcogenide Glass Data Sheet," in RPO Datasheet, (available online).
[14] "Schott Infrared Chalcogenide Glass IRG 22," in Schott Technical Datasheet, (available online).
[15] "Schott Infrared Chalcogenide Glass IRG 24," in Schott Technical Datasheet, (available online).
[16] W. Li, S. Seal, C. Rivero, C. Lopez, K. Richardson, A. Pope, A. Schulte, S. Myneni, H. Jain, K. Antoine, Role of S/Se ratio in chemical bonding of As–S–Se glasses investigated by Raman, x-ray photoelectron, and extended x-ray absorption fine structure spectroscopies, J. Appl. Phys. 98 (2005), 053503.
[17] M. Hase, P. Fons, K. Mitrofanov, A.V. Kolobov, J. Tominaga, Femtosecond structural transformation of phase-change materials far from equilibrium monitored by coherent phonons, Nat. Commun. 6 (2015) 1–6.
[18] J.S. McCloy, B.J. Riley, S. Sundaram, H.A. Qiao, J.V. Crum, B.R. Johnson, Structure-optical property correlations of arsenic sulfide glasses in visible, infrared, and sub-millimeter regions, J. Non Cryst. Solids 356 (2010) 1288–1293.
[19] M. Naftaly, A. Foulds, R. Miles, A. Davies, Terahertz transmission spectroscopy of nonpolar materials and relationship with composition and properties, J. Infrared Millim. Terahertz Waves 26 (2005) 55–64.
[20] M. Naftaly, R. Miles, Terahertz time-domain spectroscopy: a new tool for the study of glasses in the far infrared, J. Non Cryst. Solids 351 (2005) 3341–3346.
[21] M. Naftaly, R. Miles, Terahertz time-domain spectroscopy of silicate glasses and the relationship to material properties, J. Appl. Phys. 102 (2007) 1–6.
[22] M. Naftaly, R.E. Miles, Terahertz time-domain spectroscopy for material characterization, Proc. IEEE 95 (2007) 1658–1665.
[23] N.J. Tostanoski, D. Möncke, R. Youngman, S.K. Sundaram, Structure-terahertz property relationship in sodium borosilicate glasses, Int. J. Appl. Glass Sci. (2022) 1–19, https://doi.org/10.1111/ijag.16608.
[24] N.J. Tostanoski, S.K. Sundaram, Examining ceramics, glasses and composites with nondestructive terahertz radiation, Adv. Mater. Process. 180 (6) (2022) 15–21.
[25] D. Tan, K.N. Sharafudeen, Y. Yue, J. Qiu, Femtosecond laser induced phenomena in transparent solid materials: Fundamentals and applications, Prog. Mater. Sci. 76 (2016) 154–228.
[26] G.D Valle, R. Osellame, P. Laporta, Micromachining of photonic devices by femtosecond laser pulses, J. Opt. 11 (2008), 013001.
[27] R.R. Gattass, L.R. Cerami, E. Mazur, Micromachining of bulk glass with bursts of femtosecond laser pulses at variable repetition rates, Opt. Express 14 (2006) 5279–5284.
[28] A.M. Streltsov, N.F. Borrelli, Study of femtosecond-laser-written waveguides in glasses, J. Opt. Soc. Am. B 19 (2002) 2496–2504.
[29] M. Ams, G.D. Marshall, P. Dekker, M. Dubov, V.K. Mezentsev, I. Bennion, M. J. Withford, Investigation of ultrafast laser-photonic material interactions: challenges for directly written glass photonics, IEEE J. Sel. Top. Quantum Electron. 14 (2008) 1370–1381.
[30] D. Krol, Femtosecond laser modification of glass, J. Non Cryst. Solids 354 (2008) 416–424.
[31] J.D. Musgraves, K. Richardson, H. Jain, Laser-induced structural modification, its mechanisms, and applications in glassy optical materials, Opt. Mater. Express 1 (2011) 921–935.
[32] C. You, S. Dai, P. Zhang, Y. Xu, Y. Wang, D. Xu, R. Wang, Mid-infrared femtosecond laser-induced damages in As_2S_3 and As_2Se_3 chalcogenide glasses, Sci. Rep. 7 (2017) 1–9.
[33] O. Efimov, L. Glebov, K. Richardson, E. Van Stryland, T. Cardinal, S. Park, M. Couzi, J. Bruneel, Waveguide writing in chalcogenide glasses by a train of femtosecond laser pulses, Opt. Mater. 17 (2001) 379–386.
[34] G. Dong, L. Zhang, M. Peng, J. Qiu, G. Lin, F. Luo, B. Qian, Q. Zhao, Microstructural modification of chalcogenide glasses by femtosecond laser, J. Non Cryst. Solids 357 (2011) 2392–2395.
[35] M. Zhang, T. Li, Y. Yang, H. Tao, X. Zhang, X. Yuan, Z. Yang, Femtosecond laser induced damage on Ge-As-S chalcogenide glasses, Opt. Mater. Express 9 (2019) 555–561.
[36] L. Zhu, D. Yang, L. Wang, J. Zeng, Q. Zhang, M. Xie, P. Zhang, S. Dai, Optical and thermal stability of Ge-As-Se chalcogenide glasses for femtosecond laser writing, Opt. Mater. 85 (2018) 220–225.

[37] W. Ma, L. Wang, P. Zhang, Y. Xu, L. Zhu, P. Xu, F. Chen, S. Dai, Surface damage and threshold determination of Ge–As–Se glasses in femtosecond pulsed laser micromachining, J. Am. Ceram. Soc. 103 (2020) 94–102.

[38] S. Messaddeq, R. Vallée, P. Soucy, M. Bernier, M. El-Amraoui, Y. Messaddeq, Self-organized periodic structures on Ge-S based chalcogenide glass induced by femtosecond laser irradiation, Opt. Express 20 (2012) 29882–29889.

[39] L. Petit, J. Choi, T. Anderson, R. Villeneuve, J. Massera, N. Carlie, M. Couzi, M. Richardson, K. Richardson, Effect of Ga and Se addition on the "near-surface" photo-response of new Ge-based chalcogenide glasses under IR femtosecond laser exposure, Opt. Mater. 31 (2009) 965–969.

[40] K. Tanaka, Reversible photostructural change: mechanisms, properties and applications, J. Non Cryst. Solids 35 (1980) 1023–1034.

[41] K. Tanaka, Optical nonlinearity in photonic glasses, J. Mater. Sci. Mater. Electron. 16 (2005) 633–643.

[42] K. Tanaka, Midgap photon effects in As_2S_3 glass, Philos. Mag. Lett. 84 (2004) 601–606.

[43] L. Petit, N. Carlie, T. Anderson, M. Couzi, J. Choi, M. Richardson, K. Richardson, Effect of IR femtosecond laser irradiation on the structure of new sulfo-selenide glasses, Opt. Mater. 29 (2007) 1075–1083.

[44] L. Petit, N. Carlie, T. Anderson, J. Choi, M. Richardson, K.C. Richardson, Progress on the photoresponse of chalcogenide glasses and films to near-infrared femtosecond laser irradiation: a review, IEEE J. Sel. Top. Quantum Electron. 14 (2008) 1323–1334.

[45] S.K. Sundaram, J.S. McCloy, B.J. Riley, M.K. Murphy, H.A. Qiao, C.F. Windisch Jr, E.D. Walter, J.V. Crum, R. Golovchak, O. Shpotyuk, Gamma radiation effects on physical, optical, and structural properties of binary As–S glasses, J. Am. Ceram. Soc. 95 (2012) 1048–1055.

[46] O. Esenturk, J.S. Melinger, E.J. Heilweil, Terahertz mobility measurements on poly-3-hexylthiophene films: device comparison, molecular weight, and film processing effects, J. Appl. Phys. 103 (2008), 023102.

[47] T.J. Magnanelli, S. Engmann, J.K. Wahlstrand, J.C. Stephenson, L.J. Richter, E. J. Heilweil, Polarization dependence of charge conduction in conjugated polymer films investigated with time-resolved terahertz spectroscopy, J. Phys. Chem. C 124 (2020) 6993–7006.

[48] B.G. Alberding, W.R. Thurber, E.J. Heilweil, Direct comparison of time-resolved terahertz spectroscopy and Hall Van der Pauw methods for measurement of carrier conductivity and mobility in bulk semiconductors, JOSA B 34 (2017) 1392–1406.

[49] V. Kovanda, M. Vlček, H. Jain, Structure of As–Se and As–P–Se glasses studied by Raman spectroscopy, J. Non Cryst. Solids 326 (2003) 88–92.

[50] M. Iovu, E. Kamitsos, C. Varsamis, P. Boolchand, M. Popescu, Raman spectra of As_xSe_{100-x} and $As_{40}Se_{60}$ glasses doped with metals, J. Optoelectron. Adv. Mater. 7 (2005) 1217–1221.

[51] M. Iovu, E. Kamitsos, C.P.E. Varsamis, P. Boolchand, M. Popescu, Raman spectra of As_xSe_{100-x} glasses doped with metals, Chalcogenide Lett. 7 (2005) 21–25.

[52] S. Yannopoulos, K. Andrikopoulos, Raman scattering study on structural and dynamical features of noncrystalline selenium, J. Chem. Phys. 121 (2004) 4747–4758.

[53] T. Mori, S. Onari, T. Arai, Raman scattering in amorphous As-Se system, Jpn. J. Appl. Phys. 19 (1980) 1027.

[54] K. Tanaka, Amorphous Selenium and Nanostructures, Springer Handbook of Glass, 2019, pp. 645–685.

[55] A. Mao, B. Aitken, R. Youngman, D. Kaseman, S. Sen, Structure of glasses in the pseudobinary system Ga_2Se_3–$GeSe_2$: violation of chemical order and 8-N coordination rule, J. Phys. Chem. B 117 (2013) 16594–16601.

[56] K. Shportko, L. Revutska, O. Paiuk, J. Baran, A. Stronski, A. Gubanova, E. Venger, Compositional dependencies in the vibrational properties of amorphous Ge-As-Se and Ge-Sb-Te chalcogenide alloys studied by Raman spectroscopy, Opt. Mater. 73 (2017) 489–496.

[57] C. Zha, R. Wang, A. Smith, A. Prasad, R.A. Jarvis, B. Luther-Davies, Optical properties and structural correlations of GeAsSe chalcogenide glasses, J. Mater. Sci. Mater. Electron. 18 (2007) 389–392.

[58] V. Mikla, Distinct topological regimes in binary glasses, J. Phys. Condens. Matter 9 (1997) 9209.

[59] A.T. Ward, Raman spectroscopy of sulfur, sulfur-selenium, and sulfur-arsenic mixtures, J. Phys. Chem. 72 (1968) 4133–4139.

[60] T. Wagner, S. Kasap, M. Vlček, A. Sklenař, A. Stronski, The structure of As_xS_{100-x} glasses studied by temperature-modulated differential scanning calorimetry and Raman spectroscopy, J. Non Cryst. Solids 227 (1998) 752–756.

[61] M. Becucci, R. Bini, E. Castellucci, B. Eckert, H. Jodl, Mode assignment of sulfur α-S_8 by polarized Raman and FTIR studies at low temperatures, J. Phys. Chem. B 101 (1997) 2132–2137.

[62] E. Bychkov, M. Miloshova, D. Price, C. Benmore, A. Lorriaux, Short, intermediate and mesoscopic range order in sulfur-rich binary glasses, J. Non Cryst. Solids 352 (2006) 63–70.

[63] P. Chen, C. Holbrook, P. Boolchand, D. Georgiev, K. Jackson, M. Micoulaut, Intermediate phase, network demixing, boson and floppy modes, and compositional trends in glass transition temperatures of binary As_xS_{1-x} system, Phys. Rev. B Condens. Matter 78 (2008), 224208.

[64] M. Iovu, S. Shutov, A. Andriesh, E. Kamitsos, C. Varsamis, A. Seddon, D. Furniss, M. Popescu, Spectroscopical study of As_2S_3 glasses doped with Dy, Sm, and Mn, in: Proceedings of the International Semiconductor Conference, IEEE, 2002, pp. 283–286.

[65] M. Iovu, S. Shutov, A. Andriesh, E. Kamitsos, C.P.E. Varsamis, D. Furniss, A. Seddon, M. Popescu, Spectroscopic study of As_2S_3 glasses doped with Dy, Sm, and Mn, J. Non Cryst. Solids 326 (2003) 306–310.

[66] M.S. Iovu, S.D. Shutov, A.M. Andriesh, E. Kamitsos, C.P.E. Varsamis, A.B. Seddon, D. Furniss, M.A. Popescu, Spectroscopic studies of bulk As_2S_3 glasses and amorphous films doped with Dy, Sm, and Mn. XI Feofilov Symposium on Spectroscopy of Crystals Activated by Rare-Earth and Transition Metal Ions, International Society for Optics and Photonics, 2001, pp. 443–454.

[67] E. Petracovschi, B. Bureau, A. Moreac, C. Roiland, J.L. Adam, X.H. Zhang, L. Calvez, Structural study by Raman spectroscopy and ^{77}Se NMR of $GeSe_4$ and $80GeSe_2$–$20Ga_2Se_3$ glasses synthesized by mechanical milling, J. Non Cryst. Solids 431 (2016) 16–20.

[68] S. Sugai, Stochastic random network model in Ge and Si chalcogenide glasses, Phys. Rev. B Condens. Matter 35 (1987) 1345.

[69] J. Orava, T. Kohoutek, T. Wagner, Z. Cerna, M. Vlcek, L. Benes, B. Frumarova, M. Frumar, Optical and structural properties of Ge–Se bulk glasses and Ag–Ge–Se thin films, J. Non Cryst. Solids 355 (2009) 1951–1954.

[70] P. Tronc, M. Bensoussan, A. Brenac, C. Sebenne, Optical-absorption edge and Raman scattering in Ge_xSe_{1-x} glasses, Phys. Rev. B Condens. Matter 8 (1973) 5947–5956.

[71] M. Stevens, P. Boolchand, J. Hernandez, Universal structural phase transition in network glasses, Phys. Rev. B Condens. Matter 31 (1985) 981.

[72] N. Kumagai, J. Shirafuji, Y. Inuishi, Raman and infrared studies on vibrational properties of Ge–Se glasses, J. Phys. Soc. Jpn. 42 (1977) 1262–1268.

[73] R. Wang, A. Smith, A. Prasad, D.Y. Choi, B. Luther-Davies, Raman spectra of $Ge_xAs_ySe_{1-x-y}$ glasses, J. Appl. Phys. 106 (2009), 043520.

[74] G. Yang, B. Bureau, T. Rouxel, Y. Gueguen, O. Gulbiten, C. Roiland, E. Soignard, J. L. Yarger, J. Troles, J.C. Sangleboeuf, Correlation between structure and physical properties of chalcogenide glasses in the As_xSe_{1-x} system, Phys. Rev. B Condens. Matter 82 (2010), 195206.

[75] D.C. Kaseman, I. Hung, Z. Gan, B. Aitken, S. Currie, S. Sen, Structural and topological control on physical properties of arsenic selenide glasses, J. Phys. Chem. B 118 (2014) 2284–2293.

[76] R. Holomb, N. Mateleshko, V. Mitsa, P. Johansson, A. Matic, M. Veres, New evidence of light-induced structural changes detected in As–S glasses by photon energy dependent Raman spectroscopy, J. Non Cryst. Solids 352 (2006) 1607–1611.

[77] C. Zha, B. Luther-Davies, R. Wang, A. Smith, A. Prasad, R.A. Jarvis, S. Madden, A. Rode, Optical characterization of Ge-As-Se glasses containing high content of germanium, in: Proceedings of the Australian Conference on Optical Fibre Technology/Australian Optical Society, IEEE, 2006, pp. 31–33.

[78] R. Golovchak, O. Shpotyuk, J. McCloy, B. Riley, C. Windisch, S. Sundaram, A. Kovalskiy, H. Jain, Structural model of homogeneous As–S glasses derived from Raman spectroscopy and high-resolution XPS, Philos. Mag. 90 (2010) 4489–4501.

[79] J.D. Musgraves, P. Wachtel, B. Gleason, K. Richardson, Raman spectroscopic analysis of the Ge–As–S chalcogenide glass-forming system, J. Non Cryst. Solids 386 (2014) 61–66.

[80] A. Anderson, Y. Loh, Low temperature Raman spectrum of rhombic sulfur, Can. J. Chem. 47 (1969) 879–884.

[81] T. Wagner, Photo-and thermally-induced diffusion and dissolution of Ag in chalcogenide glasses thin films, J. Optoelectron. Adv. Mater. 4 (2002) 717–727.

[82] S. Sundaram, J.H.J. David Musgraves, L. Calvez, Terahertz time-domain spectroscopy of glasses. Springer Handbook of Glass, Springer, 2019, pp. 909–929.

[83] S. Sundaram, B.J. Riley, J.V. Crum, Terahertz transmission spectroscopy of chalcogenide glasses, in: Proceedings of the 33rd International Conference on Infrared, Millimeter and Terahertz Waves, IEEE, 2008, pp. 1–2.

[84] S.B. Kang, M.H. Kwak, B.J. Park, S. Kim, H.C. Ryu, D.C. Chung, S.Y. Jeong, D. W. Kang, S.K. Choi, M.C. Paek, Optical and dielectric properties of chalcogenide glasses at terahertz frequencies, ETRI J. 31 (2009) 667–674.

[85] A. Ravagli, M. Naftaly, C. Craig, E. Weatherby, D. Hewak, Dielectric and structural characterisation of chalcogenide glasses via terahertz time-domain spectroscopy, Opt. Mater. 69 (2017) 339–343.